

# Dynamical arrest in active nematic turbulence

Ido Lavi,<sup>1,2,\*</sup> Ricard Alert,<sup>3,4,5</sup> Jean-François Joanny,<sup>6,7</sup> and Jaume Casademunt<sup>2,8</sup>

<sup>1</sup>*Center for Computational Biology, Flatiron Institute, 162 5th Ave, New York, NY 10010, USA*

<sup>2</sup>*Departament de Física de la Matèria Condensada, Universitat de Barcelona, Barcelona, Spain*

<sup>3</sup>*Max Planck Institute for the Physics of Complex Systems, Nöthnitzerst. 38, 01187 Dresden, Germany*

<sup>4</sup>*Center for Systems Biology Dresden, Pfoienhauerst. 108, 01307 Dresden, Germany*

<sup>5</sup>*Cluster of Excellence Physics of Life, TU Dresden, 01062 Dresden, Germany*

<sup>6</sup>*Collège de France, Paris, France*

<sup>7</sup>*Laboratoire PhysicoChimie Curie, Institut Curie, Université Paris Sciences & Lettres (PSL), Sorbonne Universités, Université Pierre et Marie Curie (UPMC), Paris, France*

<sup>8</sup>*Universitat de Barcelona Institute of Complex Systems (UBICS), Barcelona, Spain*

(Dated: July 26, 2024)

Active fluids display spontaneous turbulent-like flows known as active turbulence. Recent work revealed that these flows have universal features, independent of the material properties and of the presence of topological defects. However, the differences between defect-laden and defect-free active turbulence remain largely unexplored. Here, by means of large-scale numerical simulations, we show that defect-free active nematic turbulence can undergo dynamical arrest. We find that flow alignment—the tendency of nematics to reorient under shear—enhances large-scale jets in contractile rodlike systems while promoting arrested flow patterns in extensile systems. Our results reveal a mechanism of labyrinthine pattern formation produced by an emergent topology of nematic domain walls that partially suppresses chaotic flows. Taken together, our findings call for the experimental realization of defect-free active nematics, and suggest that topological defects enable turbulence by preventing dynamical arrest.

Active fluids are driven internally by their own components—be they molecular motors, cells, or synthetic colloidal particles. This internal driving produces spontaneous flows, which often exhibit spatio-temporal chaos at high activity<sup>1</sup>. Chaotic flows have been observed in a variety of systems, such as bacterial suspensions<sup>2–11</sup>, sperm<sup>12</sup>, mixtures of cytoskeletal components<sup>13–22</sup>, cell monolayers<sup>23–27</sup>, and artificial self-propelled particles<sup>28–31</sup>. Although all these systems operate at low Reynolds number, for which inertia is negligible, the flows are reminiscent of classic inertial turbulence. Hence, active chaotic flows are generically referred to as active turbulence<sup>1</sup>.

Active turbulence encompasses systems with different symmetries, including polar or nematic orientational order, each exhibiting unique statistical properties<sup>1</sup>. Recent work showed that the velocity power spectrum of active nematic turbulence features scaling laws with universal exponents independent of the material properties of the fluid such as its viscosity and activity<sup>22,32,33</sup>. Whereas most experiments and simulations prominently feature topological defects<sup>34</sup>, turbulence with the same universal exponents was also found for strongly-ordered nematics in the absence of defects<sup>33</sup>. However, how the material properties and the presence or absence of defects affect other, non-universal features of the flow field remains unclear.

Here, we show that defect-free active nematic turbulence exhibits arrested patterns not seen in the presence of defects. We reveal these patterns by studying the effect of the flow-alignment parameter  $\nu$ , which characterizes the tendency of liquid crystals to reorient under shear. As expected, we find that the scaling exponent of the velocity power spec-

trum is unaffected when varying  $\nu$ , confirming its universal character<sup>1,33</sup>. Despite keeping the same scaling, we find that flow-alignment strongly affects both the strength and the spatiotemporal structure of the flows.

We identify two distinct regimes depending on the parameter combination  $\text{sign}(\zeta)\nu$ , where  $\zeta$  is the active stress parameter, with  $\zeta > 0$  for extensile and  $\zeta < 0$  for contractile stresses, respectively. We discuss the case of rod-like nematic components, for which  $\nu \leq 0$ . In the flow-aligning regime, where  $\nu < -1$ , we find that contractile nematics (with  $\zeta\nu > 0$ ) exhibit strongly chaotic flows and nematic distortions, which largely decorrelate from one another. In this regime, nematic domain walls—lines of strong variation of the director—appear, split, and dissolve, forming a dynamically reorganizing pattern (Figs. 1a to 1c, Supplementary Movie 1). In contrast, for extensile aligning nematics ( $\zeta\nu < 0$ ), we find that domain walls are strongly stabilized by the flow they entrain. The walls typically grow and branch but neither break nor merge. As walls avoid each other, they become arrested (or grid-locked) in a space-filling tree-like pattern (Figs. 1d to 1f, Supplementary Movie 2). Once arrested, the pattern exhibits slow residual dynamics that shares some features with ageing phenomena in glassy systems. The special case  $\nu = 0$  has been the focus of previous work<sup>33</sup> and is considered here as a reference. The dynamics in this case lie between these two extremes while also manifesting comparatively shorter wavelengths (Supplementary Fig. 1, Supplementary Movie 3).

We uncover that the dynamical arrest stems from the emergence of an effective topology, characterized by a set of connectivity rules for the domain walls imposed by the combined effects of activity and flow alignment. In particular, we demonstrate that, in the absence of topological defects, the arrested state is organized by local nematic structures, which we

\* [ilavi@flatironinstitute.org](mailto:ilavi@flatironinstitute.org); Present address: Flatiron Institute, New York, NY, USA

name pseudo-defects. We discuss their topological interpretation and show that they coexist with actual defects in experiments on microtubule-based active nematics. While future studies could clarify which features of defect-free active flows may also be present in active nematics with defects, achieving defect-free active nematics remains a compelling experimental challenge.

### Hydrodynamics of defect-free active nematics

We generalize our previous minimal model of active nematic turbulence<sup>33</sup> by adding flow alignment and the Ericksen stress<sup>35</sup>. We work at vanishing Reynolds number, for which momentum balance reads:

$$0 = -\partial_\alpha P + \partial_\beta (\sigma_{\alpha\beta}^a + \sigma_{\alpha\beta}^E + \sigma_{\alpha\beta}). \quad (1)$$

The pressure  $P$  enforces the incompressibility condition  $\partial_\alpha v_\alpha = 0$  of the flow field  $\mathbf{v}$ . The next two terms are the divergence of the antisymmetric part of the stress tensor, and of the symmetric Ericksen stress, respectively<sup>35,36</sup>:

$$\sigma_{\alpha\beta}^a = \frac{1}{2} (n_\alpha h_\beta - h_\alpha n_\beta), \quad \sigma_{\alpha\beta}^E = -\frac{\delta F_n}{\delta (\partial_\alpha n_\beta)} \partial_\beta n_\alpha. \quad (2)$$

These stresses arise from the elastic distortions of the director field  $\mathbf{n}$ . Distortions produce an orientational field  $h_\alpha = -\delta F_n / \delta n_\alpha = K \nabla^2 n_\alpha + h_{\parallel}^0 n_\alpha$  computed from the Frank free energy which, in the one-constant  $K$  approximation, reads

$$F_n = \int \left[ \frac{K}{2} (\partial_\alpha n_\beta) (\partial_\alpha n_\beta) - \frac{1}{2} h_{\parallel}^0 n_\alpha n_\alpha \right] d^2 \mathbf{r}. \quad (3)$$

Here, we assumed that the fluid is deep in the nematic phase so that the director field has a fixed modulus  $|\mathbf{n}| = 1$ . This constraint is imposed by the second term through the Lagrange multiplier  $h_{\parallel}^0$ . We start with a continuous director field, which precludes the generation of topological defects<sup>33,37</sup>.

The last term in Eq. (1) arises from the symmetric part of the deviatoric stress, which is given by the constitutive equation<sup>36,38–40</sup>

$$\sigma_{\alpha\beta} = 2\eta v_{\alpha\beta} - \zeta \hat{q}_{\alpha\beta} + \frac{\nu}{2} (n_\alpha h_\beta + h_\alpha n_\beta - n_\gamma h_\gamma \delta_{\alpha\beta}). \quad (4)$$

Here,  $\eta$  is the shear viscosity,  $v_{\alpha\beta} = 1/2 (\partial_\alpha v_\beta + \partial_\beta v_\alpha)$  is the symmetric part of the strain-rate tensor,  $\zeta$  is the active stress parameter, and  $\hat{q}_{\alpha\beta} = n_\alpha n_\beta - 1/2 \delta_{\alpha\beta}$  is the nematic orientation tensor defined by the director  $\mathbf{n}$ . The last term describes stresses due to flow alignment, with parameter  $\nu$ .

As in passive nematics, the dynamics of the director field are given by

$$\partial_t n_\alpha + v_\beta \partial_\beta n_\alpha + \omega_{\alpha\beta} n_\beta = \frac{1}{\gamma} h_\alpha - \nu v_{\alpha\beta} n_\beta, \quad (5)$$

where  $\omega_{\alpha\beta} = 1/2 (\partial_\alpha v_\beta - \partial_\beta v_\alpha)$  is the vorticity tensor, and  $\gamma$  is the rotational viscosity. The left-hand side is the co-rotational material derivative of the director field. On the right-hand side, the orientational field  $h_\alpha$  specifies the elastic torque acting on the director, whereas the last term captures its

reorientation due to extensional flow, i.e., the flow-alignment effect.

Nondimensionalizing the equations, we rescale length by the system size  $L$ , time by the active time  $\tau_a = \eta/|\zeta|$ , pressure by the active stress  $|\zeta|$ , and orientational field by  $K/L^2$ . To eliminate the pressure, we take the curl of Eq. (1) and obtain a Poisson equation for the vorticity  $\omega$ , which we write in terms of the stream function  $\psi$  (defined by  $v_x = \partial_y \psi$  and  $v_y = -\partial_x \psi$ )<sup>37</sup>, as  $\omega = -\nabla^2 \psi$ :

$$\nabla^2 \omega = -\nabla^4 \psi = -S \partial_\alpha \partial_\beta \bar{q}_{\alpha\beta} + R \nu \partial_\alpha \partial_\beta (\bar{q}_{\alpha\beta} h_{\parallel} - \hat{q}_{\alpha\beta} h_{\perp}) + \frac{R}{2} \nabla^2 h_{\perp} + R \epsilon_{\alpha\beta} (\partial_\alpha h_{\parallel}) \partial_\beta \theta. \quad (6)$$

Here,  $S$  is the sign of the active stresses, with  $S = \pm 1$  for extensile and contractile stresses, respectively, and  $\theta$  is the nematic director angle:  $\mathbf{n} = (\cos \theta, \sin \theta)$ . The right-hand side contains four sources of vorticity, arising respectively from active, flow-alignment, antisymmetric, and Ericksen stresses. We used the totally antisymmetric tensor  $\epsilon_{\alpha\beta}$  to define  $\bar{q}_{\alpha\beta} \equiv -\epsilon_{\alpha\gamma} \hat{q}_{\gamma\beta}$ . We also introduced the parallel and perpendicular components of the orientational field<sup>37</sup>:

$$h_{\perp} = \frac{1}{A} \nabla^2 \theta, \quad h_{\parallel} = \nu \bar{q}_{\alpha\beta} \partial_\alpha \partial_\beta \psi. \quad (7)$$

Equations (6) and (7) contain three dimensionless parameters: the activity number  $A = L^2/\ell_a^2$ , the viscosity ratio  $R = \gamma/\eta$ , and the flow-alignment parameter  $\nu$ . The activity number compares the system size  $L$  with the active length  $\ell_a = \sqrt{K/(|\zeta|R)}$  defined by the balance between active and elastic nematic stresses.

Finally, the director dynamics Eq. (5) breaks down into a component parallel to  $\mathbf{n}$ , which specifies  $h_{\parallel}$  as given in Eq. (7), and a component perpendicular to  $\mathbf{n}$ , which determines the dynamics of the nematic angle  $\theta$ <sup>37</sup>:

$$\partial_t \theta - \epsilon_{\alpha\beta} \partial_\alpha \psi \partial_\beta \theta + \frac{1}{2} \nabla^2 \psi = h_{\perp} + \nu \hat{q}_{\alpha\beta} \partial_\alpha \partial_\beta \psi. \quad (8)$$

Equations (6) to (8) give the hydrodynamics of our active fluid in terms two fields: the angle  $\theta$  and the stream function  $\psi$ .

We numerically integrate Eqs. (6) to (8) in a square with periodic boundary conditions using a hybrid numerical scheme that combines a pseudo-spectral method for Eq. (6) with the finite element method for Eq. (8) (Methods A). Unless otherwise specified, we set  $R = 1$  and  $A = 3.2 \times 10^5$ , for which the system was shown to develop large-scale active turbulence when  $\nu = 0$ <sup>33</sup>. The dynamics are invariant under the transformation ( $\nu \rightarrow -\nu$ ,  $S \rightarrow -S$ ,  $\theta \rightarrow \theta \pm \pi/2$ ), meaning that changing the signs of  $\nu$  and  $S$  simultaneously leaves the system invariant up to a rotation<sup>37,41,42</sup>.

### Strong large-scale turbulence

We first study the case  $S\nu > 1$ , realized with contractile flow-aligning rods ( $S = -1$  and  $\nu = -1.1$ ). We find a chaotic flow field with vortices at many scales and strong (albeit transient) large-scale jets (Fig. 1a). These flow patterns stem from long-range hydrodynamic interactions and are largely uncorrelated with the director field (Fig. 1c), which also evolves

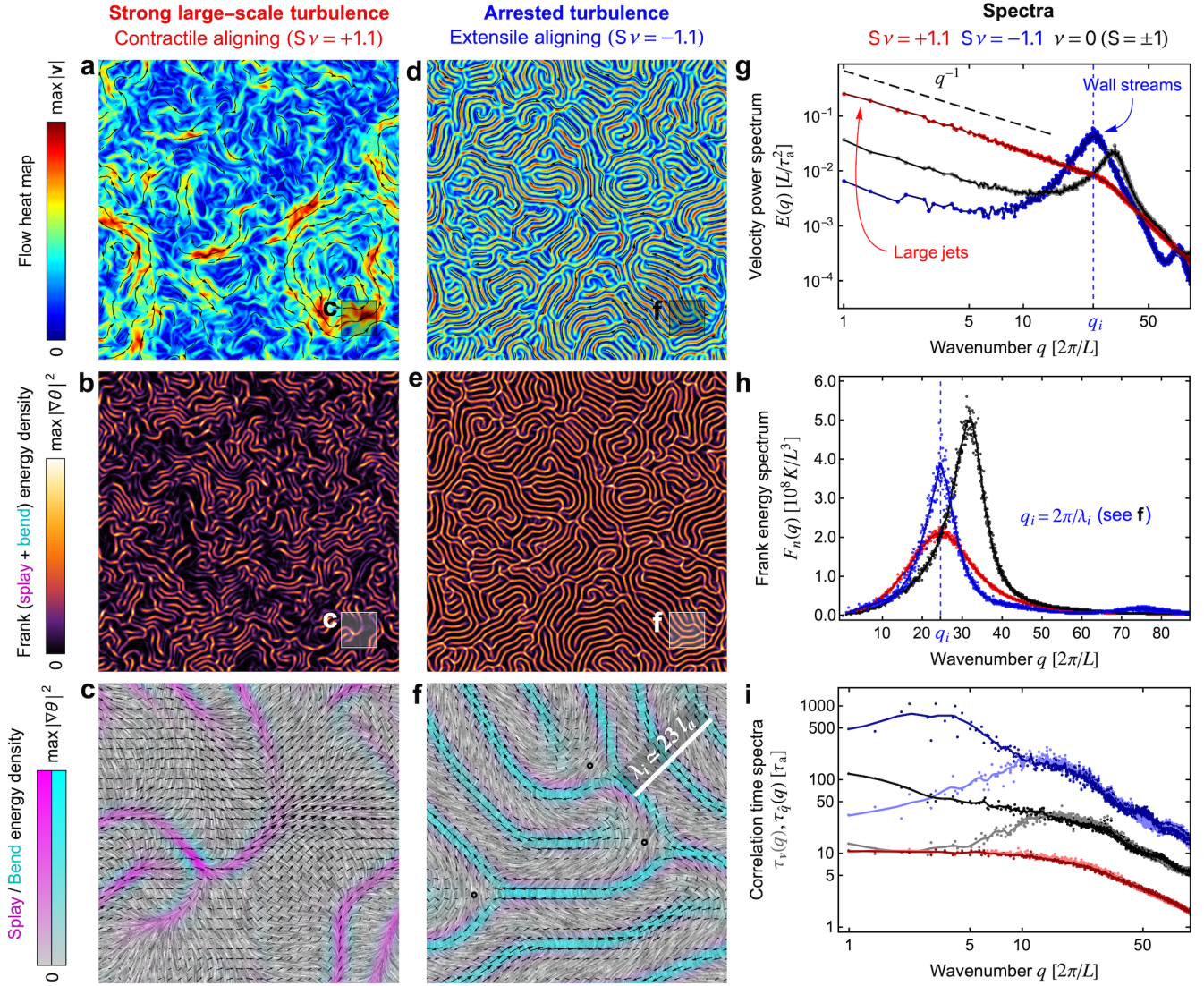


**Figure 1 | Strong and arrested regimes of active nematic turbulence.** **a–f**, Snapshots from simulations of defect-free active nematic turbulence in contractile (**a–c**) and extensile (**d–f**) flow-aligning systems. Parameter values were set to  $R = 1$ ,  $\nu = -1.1$ , and  $A = 3.2 \times 10^5$ . Top panels (**a,d**) show the flow field; black curves are streamlines, and the color indicates the speed (see [Supplementary Movies 1 and 2](#)). Middle panels (**b,e**) show the Frank free energy density  $\sim |\nabla\theta|^2$ , with high-intensity lines corresponding to nematic domain walls (see [Supplementary Movies 1 and 2](#)). Bottom panels (**c,f**) are zooms highlighting the type of nematic distortion as well as the interplay between nematic walls and flows. The gray-scale background is the line integral convolution representation of the director field  $\mathbf{n}$ . Magenta and cyan intensities respectively represent splay  $(\nabla \cdot \mathbf{n})^2$  and bend  $|\nabla \times \mathbf{n}|^2$  contributions to the Frank energy density. The black arrows represent the flow field  $\mathbf{v}$ , which localizes along the nematic walls in the arrested regime. White scale bar represents the selected wavelength  $\lambda_i$ . **g–i**, Spectra characterizing fully-developed active nematic turbulence (see details in [Methods B](#)). The lines in (**h,i**) represent a smoothed (Gaussian) interpolation of the computed data points. We compare the flow-aligning contractile (red, as in **a–c** and [Supplementary Movie 1](#)) and extensile (blue, as in **d–f** and [Supplementary Movie 2](#)) cases with the  $\nu = 0$  case (black, as in [Supplementary Fig. 1](#) and [Supplementary Movie 3](#)), for which contractile and extensile stresses are equivalent up to a rotation<sup>37,41,42</sup>. **g**, Velocity power spectrum on a log-log scale, showing (i) the universal low- $q$  scaling law and (ii) the distinct organization of flows across scales in the different cases. The wider scaling regime in the contractile case captures the strong large-scale jets (see **a**). The peak in the extensile case is representative of wall streams (see **d**). **h**, Frank energy spectrum, showing that (i) the selected wavelength (peak position) depends on  $\nu$  but not on the sign of active stress, and (ii) the peak width depends on the sign of active stress when  $\nu \neq 0$ . **i**, Spectrum of correlation times associated with the flow  $\mathbf{v}$  (light colored points and lines) and the nematic tensor  $\hat{q}_{\alpha\beta}$  (darker points and lines). This log-log plot reveals strong differences in decay times between the regimes, as well as the differences between the flow and nematic tensor within a regime. Correlation times are extracted from exponential fits to the corresponding space-time autocorrelation functions in Fourier space (see [Methods B](#)).

chaotically. The Frank energy density concentrates along domain walls (Figs. 1b and 1c)—well-known regions of strong orientation gradients<sup>43–45</sup>. Such walls feature a typical separation length, corresponding to the peak position in the Frank energy spectrum (Fig. 1h, red), coinciding with the peak of the nematic tensor power spectrum (Supplementary Fig. 2, red). Compared with the  $\nu = 0$  case<sup>33</sup>, the nematic pattern in the  $S\nu > 1$  regime appears more broken, with fragmented walls coexisting with wall-free regions (dark patches in Fig. 1b). As a consequence, the total Frank free energy is smaller, and its peak is shifted to larger scales (Fig. 1h, red). A dynamically-rearranging pattern emerges as walls spontaneously appear, split, and dissolve (Supplementary Movies 1 and 4, left). Both the flows and the nematic tensor are very dynamic, as confirmed by their short correlation time at all length scales (Fig. 1i, red).

In recent work we have shown that, for  $S\nu > 1$ , both the quiescent state with uniform orientation and the flowing state with splaying domain walls are non-linearly unstable against one-dimensional modulations<sup>37</sup>. Thus, strong enough perturbations can trigger sudden transitions between these states. For this reason, we assert that domain wall patterns can be disrupted by the strong turbulent flows. In the two-dimensional simulations shown here, we observe the coexistence of uniform and wall-laden patches that continuously rearrange. We conclude that the metastability associated with this regime strongly enhances the chaotic flows, particularly at large-scales, as indicated by the wide  $q^{-1}$  scaling regime in Fig. 1g, red.

### Arrested turbulence

We now study the case  $S\nu < -1$ , realized with extensile flow-aligning rods ( $S = +1$  and  $\nu = -1.1$ ). While the system still evolves chaotically, large-scale flows are much weaker than in the other cases, with the  $q^{-1}$  power law spanning a narrower range of scales (Fig. 1g, blue). Rather than large-scale jets, the dominant flows are at shorter length scales, as indicated by the enhanced peak of the velocity power spectrum (Fig. 1g, blue). These smaller-scale flows form streams that are strongly localized along the bending domain walls where the active stress gradients are larger (Figs. 1d to 1f).

In contrast to the non-arrested case, here a connected wall pattern extends across the entire system (Fig. 1e). The Frank free energy spectrum is more narrowly peaked at the characteristic length scale (Fig. 1h, blue), compared to the non-arrested case (Fig. 1h, red). The same peak is also prominent in the nematic tensor power spectrum (Supplementary Fig. 2, blue). Strikingly, the nematic wall pattern becomes far less dynamic; the walls and their associated streams become locked in a tree-like pattern. We term this phenomenon dynamical arrest. The weak large-scale chaotic flows make the pattern fluctuate only slightly (Supplementary Movies 2 and 4, right). The dynamical arrest manifests in much longer correlation times, especially of the nematic tensor field at large scales (Fig. 1i, blue). The tree-like pattern of domain walls is characterized by unique connectivity properties, which we elaborate on later. We conclude that, in the absence of topological defects, the combined effects of extensile stress and

rod-like flow-alignment give rise to the arrest of active nematic turbulence.

### Wall dynamics and mechanism of arrest

To understand the mechanism of arrest, we note that the spontaneous-flow instability, which ultimately drives turbulence, generates shear flow<sup>46</sup>. This shear produces antiparallel flows that concentrate along the nematic walls<sup>33,37,41,42,46,47</sup>. The walls are directed lines, with their direction defined by the vector  $(\partial_y\theta, -\partial_x\theta)$ , which is perpendicular to the gradient of the angle and coincides with the flow direction in the arrested regime.

Quasi one-dimensional wall patterns tend to coarsen, leading to larger domains (Fig. 2a and Supplementary Movie 4, right). Since the director orientation is roughly uniform within such domains, the same instability prompts distortions in a perpendicular direction<sup>33,47</sup>. This process induces sequential ‘zig-zag’ instabilities, leading to wall branching and progressively smaller domains, until a characteristic wavelength is selected (Fig. 2b and Supplementary Movie 4, right)<sup>19,33</sup>. When an open end of a branch approaches another wall perpendicularly, it is deflected and becomes antiparallel to that wall. The growth of branches typically stops when they are blocked by a preexisting branch point. Ultimately, these dynamics lead to a grid-locked pattern (Fig. 2c and Supplementary Movie 4, right).

When a growing wall is trapped by a branch point, the outflowing stream at the end point of the wall is diverted to both sides so that material can join the antiparallel streams of neighbouring walls (see Fig. 1f, around the black circles). In other words, a stagnation point is formed as flows arrive in the direction of the growing wall and leave in the perpendicular direction, to which rods tend to align. For bending walls—induced by an extensile stress—the director is perpendicular to the wall and therefore aligned with the extensional axis of the flow. We thus postulate that the structure around the stagnation point acts as a trap, and its stability is key to understanding how flow alignment promotes the arrest of active turbulence.

### The nodes of nematic domain walls define pseudo-defects

The domain walls emerging in our system are typically of a single type (either splaying or bending, see Figs. 1c and 1f). Such walls generically feature three types of nodes:

1. Startpoints, with one outgoing wall and no incoming wall (Fig. 3a),
2. Branchpoints, with one incoming wall and two outgoing walls (Fig. 3b),
3. Endpoints, with one incoming wall and no outgoing wall (Fig. 3c).

A node with two incoming walls and one outgoing wall is only possible by combining different wall types (Supplementary Fig. 3). We further note that startpoints are very common in the non-arrested (contractile aligning) regime but become increasingly rare over time in the arrested (extensile aligning) regime.

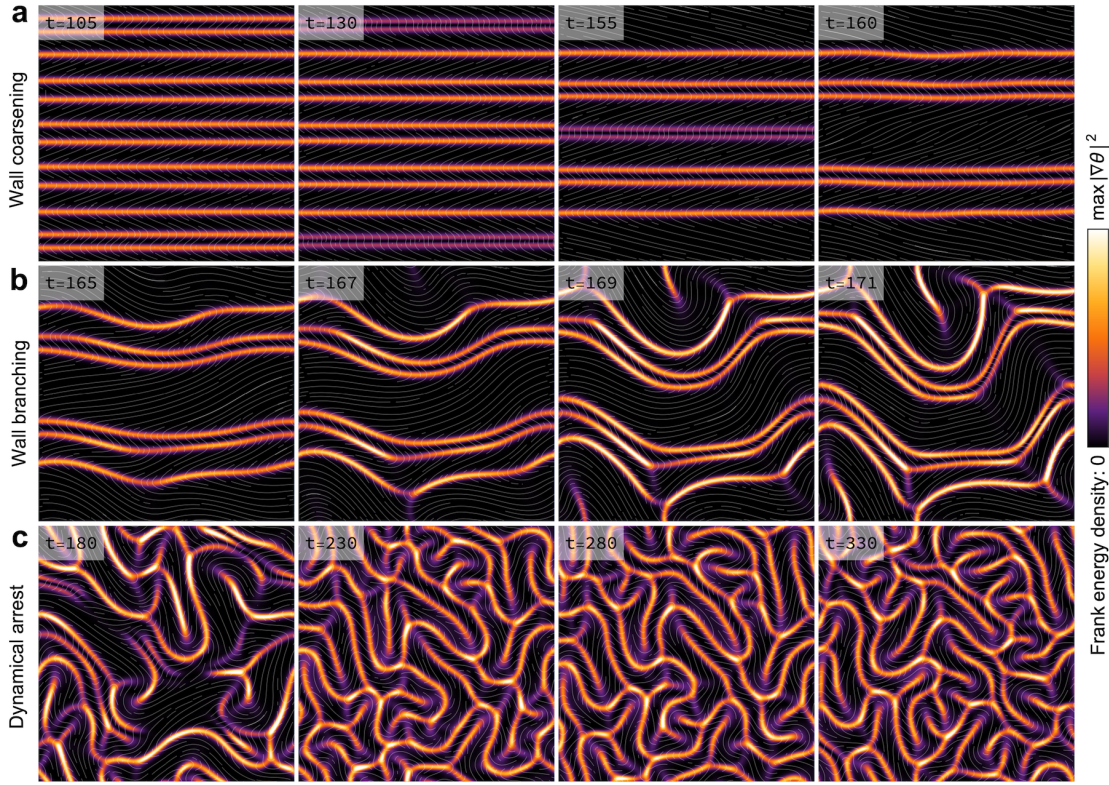


**Figure 2 | Wall coarsening, branching, and dynamical arrest.** Sequential snapshots from a single simulation in the extensile flow-aligning regime, showing the coarsening of bending walls (a, top row), the zigzag instability of the coarsened configuration, followed by wall branching and rapid tip growth (b, second row), and the evolution towards the arrested tree pattern (c, bottom row). The initial condition was set to a striped pattern of wavelength that matches the typical length selected in the chaotic regime (see first and final panels). A perturbation along the  $y$ -axis triggers the coarsening of one-dimensional stripes, confirming that straight anti-parallel walls do not have a preferred separation. The length selected in the tree-like pattern is determined by two-dimensional interactions, with growing branches avoiding preexisting walls. Parameter values are:  $R = 1$ ,  $S = 1$ ,  $\nu = -1.1$ , and  $A = 19692$  (chosen so that the system size roughly equals six times the selected wavelength).

We define these three types of points as pseudo-defects. Unlike proper topological defects, they are not phase singularities of the director field, and they do not carry a topological charge. Nevertheless, the director varies around them in a manner that resembles true nematic defects, except for its sharp counter variation across the walls. We thus assign the nodes a pseudo-charge, defined as the number of turns of the director along a path that surrounds the pseudo-defect, excluding the sharp variation across all intersecting walls (Figs. 3a to 3c). The excluded walls in this definition are analogous to the so-called Dirac strings, which are constructs that enable magnetic monopoles in Maxwell’s equations<sup>48</sup> (see discussion in [Supplementary Note](#)). With this definition, endpoints have a positive pseudo-charge  $+Q$  (Fig. 3c) and both startpoints and branchpoints have pseudo-charge  $-Q$  (Figs. 3a and 3b). The pseudo-charge depends on  $\nu$ . For  $S\nu > -1$ , we have  $Q \simeq 1/2$ , while for  $S\nu \leq -1$ , we have  $Q \simeq \frac{1}{2} \left[ 1 - \frac{1}{\pi} \arccos(|\nu|^{-1}) \right]$  (see details in [Supplementary Note](#)). The total pseudo-charge contained in a closed domain is  $mQ$  where  $m$  is the difference between the number of walls crossing the path inwards and outwards ([Supplementary Note](#)). All pseudo defects have polarity, defined by the direction of the

outgoing wall for startpoints (Fig. 3a) and the direction of the incoming wall for branchpoints and endpoints (Figs. 3b and 3c).

The topological pseudo-charge is preserved by the dynamics of the director. Pseudo-defects with opposite charges are created in pairs and annihilated in pairs (Figs. 3d to 3f), similarly to actual nematic defects. A wall endpoint cannot merge with a preexisting wall. Instead, it can connect with a startpoint ahead of it (the inverse process of Fig. 3e) or, through wall shrinkage, it can annihilate with the nearest negative pseudo-defect it is *connected to* (the inverse processes of Figs. 3d and 3f). Notably, this nearest connected point does not need to be its birth pair and may be quite a long distance away, as we often observe in the arrested regime. In addition to pair birth and annihilation, negative pseudo-defects can transition from one to the other while conserving the pseudo-charge (Fig. 3g and its inverse process). In another pseudo-topological transition, connected branchpoints can exchange branches (Fig. 3h). This process is akin to a T1 transition in foams and tissues, except that our lines are directed, and branching nodes are restricted to having one incoming wall and two outgoing walls. As a result, T2 transitions are not

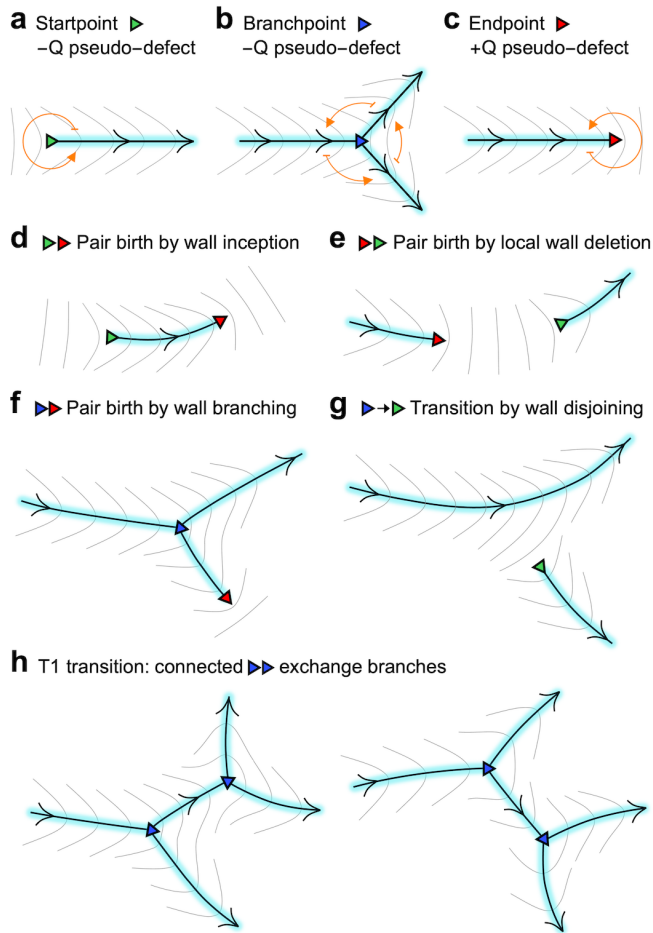


**Figure 3 | Domain wall nodes and their pseudo-topology.** In all diagrams, black directed lines represent nematic bending walls, with gray lines tracing the director and cyan indicating the bending energy. **a–c**, Nodes are either startpoints (green, negative pseudo-defects), branchpoints (blue, negative pseudo-defects), or endpoints (red, positive pseudo-defects). The orange curves illustrate the paths excluding walls used to define the pseudo-charge (Supplementary Note). **d–e**, Two ways in which a startpoint-endpoint pair of opposite charge can be born. The inverse processes of **(d)** (complete wall dissolution) and **(e)** (local wall completion) result in the annihilation of such pairs. **f**, Wall branching gives birth to a branchpoint-endpoint pair, also of opposite charge. A connected pair may annihilate via branch retraction. **g**, A branchpoint **(b)** transitions into a startpoint when one outgoing wall disjoins. The inverse process corresponds to a startpoint **(a)** joining with a bare wall. **h**, Connected branchpoints can shrink their connecting branch, transiently creating a  $-2Q$  pseudo-charged structure, exchange outgoing walls and extend again in the perpendicular direction.

possible.

One can imagine other transitions between wall nodes that are permitted by the pseudo-topological rules. To the best of our understanding, such processes can be viewed as either analogues or sequences of the basic transitions shown in Fig. 3. Moreover, all processes involving startpoints are rare

in arrested wall networks.

### Motifs of arrested wall networks

In the arrested turbulence regime (with  $S\nu < 0$ ), the processes of wall folding, branching, extension, and arrest produce a directed tree-like network of self-avoiding walls (Fig. 2). This network does not form closed loops in a simply-connected domain because such a loop would enclose a topological charge of 1, implying actual nematic defects, which our system forbids.

We find that endpoints propagate rapidly in the direction of their polarity, until they are blocked by other walls. Startpoints, on the other hand, move quickly in the opposite direction of their polarity until their wall dissolves or they merge with another wall, transitioning into a branchpoint. Unlike endpoints and startpoints, branchpoints do not move in the direction parallel or antiparallel to their polarity. Rather, when they are created (Fig. 3f), they tend to deflect only slightly in the direction of the newly formed branch (Fig. 2b). Hence, in the sense of their mobility, endpoints are akin to actual  $+1/2$  nematic defects and branchpoints are similar to  $-1/2$  defects, which are not mobile.

Ultimately, the pseudo-defects—primarily endpoints and branchpoints—maintain a steady distance from neighbouring walls and organize into motifs like those shown in Figs. 4a to 4d. A frequent motif, which we call the anchoring motif (Fig. 4a), is the one discussed previously in relation to the stagnation points in Fig. 1f. We postulate that this structure might be particularly stable because neighbouring walls are anti-parallel, as promoted by the spontaneous-flow instability. In contrast, the other basic motifs (Figs. 4b to 4d) feature some neighbouring walls that are parallel. For smaller system sizes, closer to the transition to chaos, we observe that only the anchoring motifs survive in the long time limit. For large system sizes, a variety of composite structures combining all types of motifs can emerge and persist for long times. One such structure is shown in Fig. 4e.

We identified bending domain walls, pseudo-defects and our motifs in images and videos of microtubule-based active nematics<sup>15,49–52</sup> (Figs. 4f to 4g). In Fig. 4f, the spontaneous-flow instability leads to the growth of bending domain walls and the emergence of pseudo-defects. These tend to organize in interlaced anchoring motifs, which are also frequently observed in our simulations. In Fig. 4g, pseudo-defects are seen to coexist with actual nematic defects (white). Since the latter may also act as origin points or termination points of walls, there may be an interesting interplay between both types of structures in organising the dynamics of the system. It is important to note that in these experimental examples the system does not maintain an arrested state. We expand on this aspect further in the final discussion.

### Ageing dynamics

The dynamics of active nematics are not relaxational, and the arrested patterns reported here co-exist with a background of weak large-scale chaotic flows. Nevertheless, these dynamics share interesting similarities with relaxational systems that exhibit frustration. In particular, trapping motifs

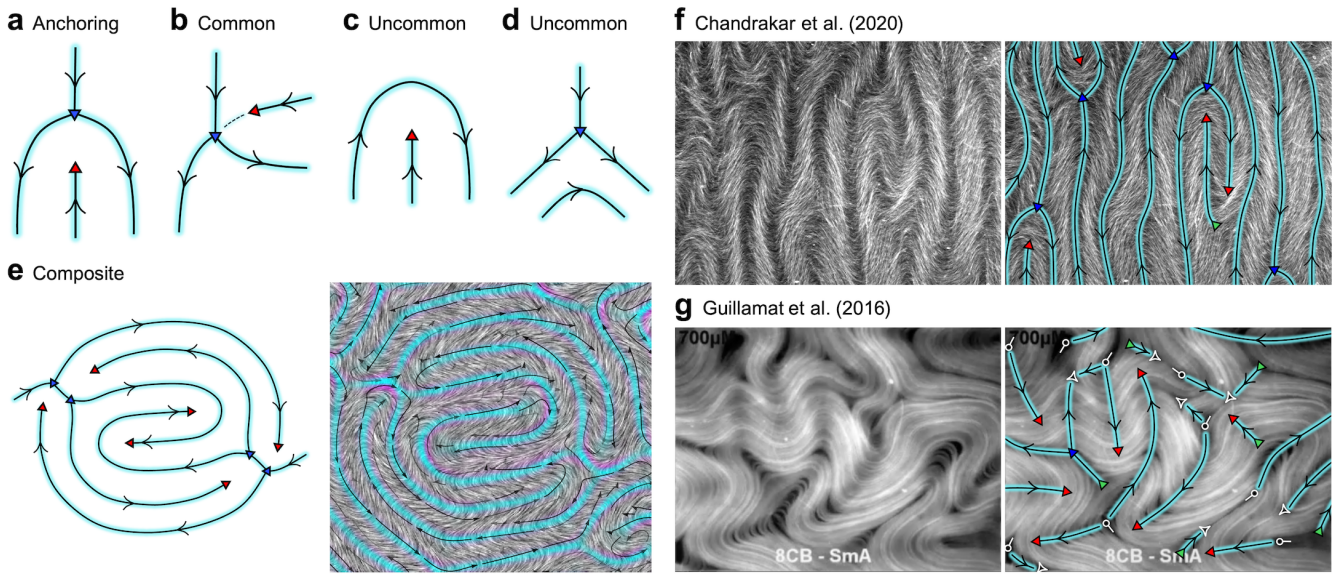


**Figure 4 | Motifs of arrested wall networks and experimental snapshots of microtubule-kinesin active nematics.** In all diagrams, lines, nodes and colors are as defined in Fig. 3. **a–d**, Basic network motifs. The anchoring motif (**a**) is made of an endpoint and branchpoint that meet head-on, with the endpoint trapped between the two outgoing walls of the branchpoint. In motif (**b**) the endpoint meets the branchpoint from one of its sides, i.e. between the incoming wall and an outgoing wall. The dashed line traces a weak distortion, indicating that the wall associated with the endpoint tends to align its direction with the outgoing wall on the opposite side of the branchpoint. The motifs (**c,d**) involve a single pseudo-defect interacting with a bare wall. These, along with (**b**), do not follow the tendency to have strictly antiparallel walls. **e**, Composite motif schematic (left) and one formed spontaneously in a simulation (right). The stream plot on the right represents the flow, with black indicating maximal  $|\mathbf{v}|$  and full transparency indicating  $|\mathbf{v}| = 0$ . The gray background is the line-integral-convolution representation of the nematic director  $\mathbf{n}$ . Parameter values and color legend for splay and bend distortions are as in Fig. 1f. **f–g**, Raw fluorescence images from experiments (left panels) and overlaid schematic drawings (right panels) depicting domain walls, pseudo-defects and actual  $\pm 1/2$  defects in white. **f**, Taken from a movie in<sup>49</sup> (courtesy of Guillaume Duclos), which shows the evolution of the microtubule-based nematic following the bending instability of the aligned state. **g**, Taken from a movie in<sup>50</sup> (courtesy of Pau Guillaumat), which shows a turbulent transient with all types of pseudo-defects and actual nematic defects. Note how walls may also originate from true  $+1/2$  defects and be absorbed by true  $-1/2$  defects.

(Figs. 4a to 4b) might promote arrest similarly to how cages and locally-favoured structures promote arrest in gels and glasses<sup>53–55</sup>. Additionally, the wall network undergoes a slow relaxation that is reminiscent of the ageing of gels and glasses. The background turbulent-like flows produce small low- $q$  fluctuations that slowly evolve the pattern. This includes jittering the walls and inducing some pseudo-topological transitions in the network; primarily those depicted in Figs. 3f to 3h and their inverse processes. Crucially, these represent a highly restrictive subset of transitions compared to the full range of processes enabled when startpoints are more prominently present. Through this fluctuating process, we find that the number of pseudo-defects gradually decreases (Fig. 5, Supplementary Movie 5), mostly via annihilation of connected branchpoint-endpoint pairs. As some walls shrink and disappear from the network, others extend, thereby maintaining the selected wavelength. At long times ( $\sim 10^3 \tau_a$ ), the evolution slows down and the number of pseudo-defects seems to approach a steady state (Fig. 5c).

#### The tree-like wall network encloses unicursal labyrinths

When there are no startpoints, the gaps between the walls form unicursal labyrinths of a type known as meanders, de-

finied by having a single path with neither bifurcations nor dead ends. A typical wall network encloses a small and even number of such labyrinths, with each one closing on itself through the periodic boundaries, i.e., through the hole of the torus, which is not a simply-connected domain (Figs. 6a and 6b). On the other hand, the wall network bounding these unicursal paths forms a maze, defined as having multiple bifurcations and dead ends, corresponding to our branchpoints and endpoints. The specific walls separating the different unicursal labyrinths are initially generated by the spontaneous-flow instability. There are as many of these *primary walls* as there are unicursal labyrinths, and they also close on themselves through the periodic boundaries. Since primary walls are the only paths on the network that avoid dead ends, they can be thought of as the solutions to the maze.

Paintings, rock-carvings, ornaments and monuments depicting unicursal labyrinths predate recorded history and have remained common in artistic and spiritual designs<sup>56</sup>. Renowned examples include the Cretan labyrinth of Greek mythology (Fig. 6c), and the labyrinth decorating the floor of Chartres cathedral (Fig. 6d). However, unlike ours, these and most other Labyrinth designs feature a dead end in the center. On the other hand, meanders (Fig. 6e) may close on

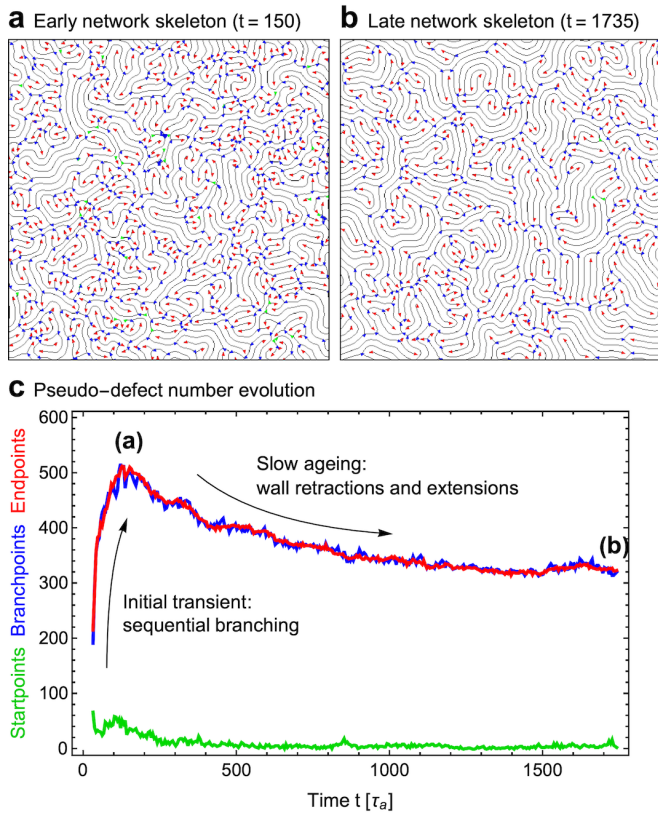


**Figure 5 | Ageing of the arrested wall network.** **a,b**, Skeleton of the domain walls (black) with startpoints, branchpoints and endpoints (green, blue and red triangular nodes) at an early time **(a)** and a late time **(b)**. The detection of the network skeleton and its nodes is described in [Methods C](#), [Supplementary Fig. 4](#). **c**, Evolution of the number of startpoints (green), branchpoints (blue) and endpoints (red). In the initial transient, sequential ‘zig-zag’ instabilities result in the proliferation of both branchpoints and endpoints. Once the wall pattern establishes a wavelength, the system ages slowly as some endpoints retract and annihilate with their connected branchpoint, while others extend ([Supplementary Movie 5](#)). Throughout the simulation, there are frequent transitions between branchpoints and startpoints, though the number of startpoints remains low. Additionally, the detection algorithm is not perfect, occasionally misidentifying endpoints or branchpoints as startpoints and vice versa. Parameter values were set to  $R = 1$ ,  $S = 1$ ,  $\nu = -0.9$ , and  $A = 3.2 \times 10^5$

themselves through the hole of the torus. In pattern-forming systems, unicursal labyrinths are rare. They were obtained under special conditions in simulations of a modified Swift-Hohenberg equation<sup>57</sup>, and in experiments with ferrimagnetic garnet films in specific experimental protocols<sup>58–60</sup> ([Fig. 6f](#)). In our case, they result from an emerging topology of domain wall networks and they occur spontaneously and generically in the arrested regime.

## Discussion

In this work, we showed that flow alignment—the tendency of liquid crystals to reorient under shear—dramatically influ-

ences the spatiotemporal structure of defect-free active nematic turbulence ([Fig. 1](#)). For contractile flow-aligning active nematics, the chaos is characterized by fragmented nematic patterns, reduced total Frank free energy, and strong self-similar flows across a broad range of scales. We associate this strong large-scale turbulence to the underlying metastability of uniform and wall-laden states<sup>37</sup>. On the other hand, despite their chaotic dynamics, we find that extensile aligning active nematics self-organize into an arrested tree-like pattern of nematic domain walls, with the flow strongly channeled along them ([Figs. 1d](#) and [1e](#)). This finding reveals a mechanism of pattern formation mediated by active turbulence, complementing those found in other studies<sup>61–63</sup>. In particular, our patterns enclose unicursal labyrinths ([Fig. 6](#)), which do not appear spontaneously in other pattern-forming systems.

The labyrinths in [Fig. 6b](#) span the entire system, but how far can they possibly extend? Further increasing the system size widens the range of chaotic self-similar flows, identified by the  $q^{-1}$  scaling of the velocity power spectrum ([Fig. 1g](#), blue). These flows become stronger at larger scales, and hence they could potentially disrupt the arrested wall pattern for sufficiently large systems. At the scale where chaotic large-scale flows become as strong as the wall streams, which sustain the domain walls, the tree-like network could lose its connectivity and fluctuate more strongly. In fact, for the system size studied here, this competition between wall streams and chaotic large-scale flows is observed for  $\nu = 0$  ([Fig. 1g](#), black). In this case, we observe a wall network, locally similar to the arrested ( $S\nu = -1.1$ ) pattern, but sporadically fractured in random positions ([Supplementary Fig. 1](#), [Supplementary Movie 3](#)). In line with our hypothesis, the fractured areas where the wall pattern dissolves (dark regions in the Frank free energy density) appear to coincide with hot spots of large-scale flows. The wall pattern is subsequently restored at fractured regions because large jets are not persistent, as shown by the low correlation times of low- $q$  flow in [Fig. 1i](#), dashed black.

The arrested state does not show long-range correlations in the nematic order parameter ([Supplementary Fig. 2](#), blue). This is reminiscent of some passive systems, such as spin ice, that feature frustration in the absence of long-range geometrical correlations<sup>64</sup>. Similarly, our pattern features short-range disorder and is yet connected over long distances. Therefore, we propose that the unicursal labyrinths exhibit a form of long-range topological order stemming from emergent connectivity rules associated with the folding, branching, extension and self-avoidance of the domain walls.

In the fully-developed turbulent state, both the arrested and non-arrested regimes manifest a selected wavelength. This wavelength is significantly greater than the active length  $l_a$  ([Fig. 1f](#)), and it also exceeds the critical wavelength of the spontaneous-flow instability. The wavelength selection mechanism is inherently nonlinear and two-dimensional; it is based on a balance between the coarsening of local striped patterns, which tends to enlarge the characteristic wavelength ([Fig. 2a](#)), and the bending and folding of walls that tends to reduce it ([Fig. 2b](#)). A deeper understanding of the selection mechanism and its dependence on parameters remains an open question.

Whereas our model is defect-free, most experiments and

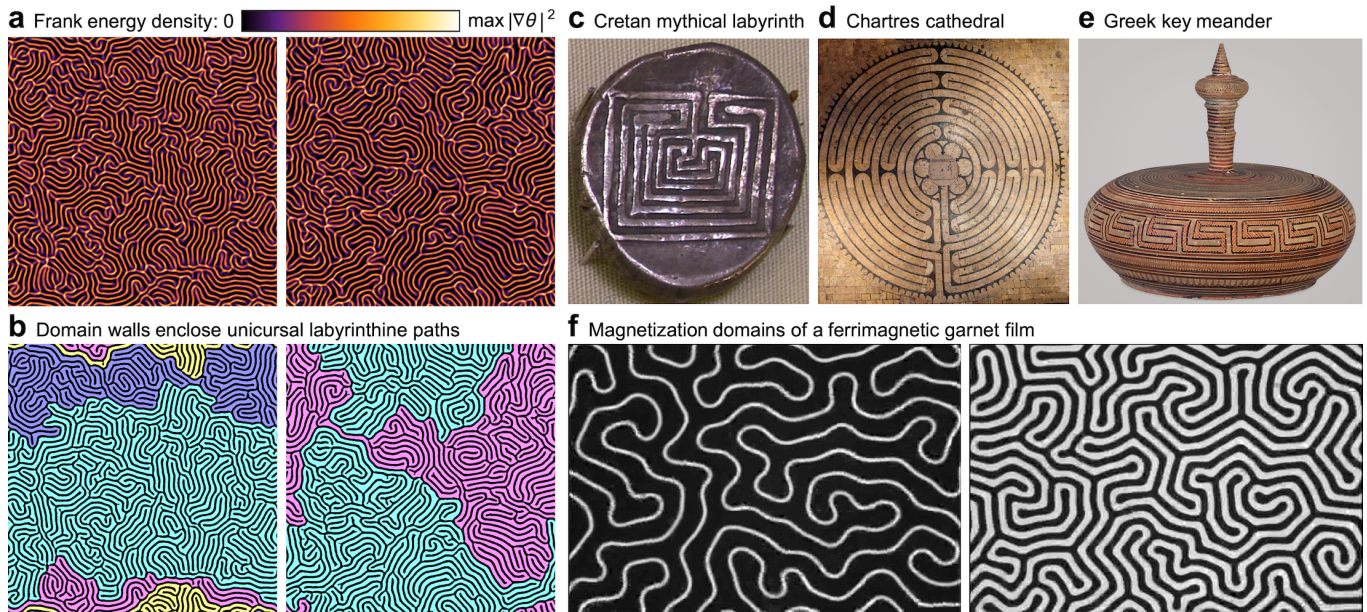


**Figure 6 | Unicursal labyrinths.** **a**, Two examples of arrested tree-like patterns formed by domain walls, with  $S\nu = -0.9$  (left) and  $S\nu = -1.1$  (right). **b**, Processed negatives of **(a)** showing how domain walls (black) enclose a small and even number of unicursal labyrinths (4 connected regions on the left, 2 on the right) that span the entire system (Methods C, Supplementary Fig. 5). The walls separating different labyrinths are self-connected across the periodic boundaries, unlike all other branches which feature endpoints. **c**, The mythical labyrinth of Crete, shown on a silver coin from around 400 BC (by AlMare, reproduced from Wikimedia Commons, creative commons license CC BY-SA 3.0). **d**, The labyrinth in the Chartres cathedral (courtesy of Père Emmanuel Blondeau and the secretariat de la Cathédrale Notre-Dame de Chartres). **e**, Meander pattern known as the Greek key encircling a box (pyxis) from around 850 BC (reproduced from the Metropolitan Museum of Art). **f**, Out-of-plane magnetization domains of a ferrimagnetic garnet film, with black and white regions indicating opposite magnetizations. The amplitude of an external magnetic field favouring the black domain is gradually reduced from left to right, resulting in growth by folding of the white unicursal domain. Frames are desaturated snapshots from a video courtesy of Pietro Tierno.

simulations in active nematics have been conducted in defect-laden regimes. Yet, the physics of the two regimes may intersect, perhaps similarly to the crossovers found in polar fluids<sup>65,66</sup>. Actual nematic defects tend to nucleate along nematic domain walls, thereby dissolving them<sup>34,43–45</sup>. Additionally, nematic constituents such as microtubules are depleted at defects (Fig. 4g), which lowers their energy cost and favours their nucleation<sup>67</sup>. The frequent dissolution of domain walls by defects explains why, in the instances where our motifs can be seen (Figs. 4f to 4g), they do not last for long. We therefore propose that, in addition to their well-known role as *drivers* of turbulence by generating vorticity<sup>32</sup>, defects also play an important role as *enablers* of stronger turbulent flows by breaking the potential grid-lock, i.e., preventing dynamical arrest.

Directly testing our predictions for defect-free active nematics presents an experimental challenge. This would require searching for active materials for which the nucleation of defect pairs were significantly more costly than in the experimental realizations studied thus far. Defect-free active turbulence should be achievable for sufficiently large system sizes  $L$ , ensuring large dimensionless activity  $A = (L/\ell_a)^2 \gg 1$ , while keeping the defect-core size  $a$  small enough ( $\ell_a \gg a$ ) to preclude defect nucleation.

In conclusion, our study of defect-free active nematic tur-

bulence highlights the crucial role of topology beyond the existence of topological defects. We argue that the connectivity of domain walls, the existence of pseudo-defects, and their interactions are key to understanding the dynamics of active nematics, from strong large-scale turbulence to dynamical arrest. Furthermore, when true defects are present, their interplay with pseudo-defects likely adds another intriguing layer of complexity. Our results open new avenues for experimental analysis and design, particularly in tracing the intricate web of domain walls, their orientation, and their nodes.

### Acknowledgments

Funding from the Spanish Ministry for Science and Innovation MICCINN/FEDER (PID2022-137713NB-C22 to IL and JC) and the Generalitat de Catalunya (AGAUR SGR-2021-00450 to IL and JC and ‘ICREA Academia’ award to JC) is acknowledged. IL acknowledges support from the Flatiron Institute, part of the Simons Foundation. RA thanks the Isaac Newton Institute for Mathematical Sciences for support and hospitality during the Programme *New Statistical Physics in Living Matter*, supported by EPSRC Grant Number EP/R014604/1, when work on this paper was undertaken.

### Author contributions

IL performed all the simulations and analyses. JC conceived and supervised the research. IL and JC developed

the theory. All authors discussed the results and wrote the manuscript.

### Competing interests

The authors declare no competing interests.

### Data and code availability

The data and code supporting the findings of this study are available from the corresponding author, IL, upon reasonable request.

1. Ricard Alert, Jaume Casademunt, and Jean-François Joanny, “Active Turbulence,” *Annu. Rev. Condens. Matter Phys.* **13**, 143–170 (2022).
2. Christopher Dombrowski, Luis Cisneros, Sunita Chatkaew, Raymond E. Goldstein, and John O. Kessler, “Self-Concentration and Large-Scale Coherence in Bacterial Dynamics,” *Phys. Rev. Lett.* **93**, 098103 (2004).
3. Luis H. Cisneros, Ricardo Cortez, Christopher Dombrowski, Raymond E. Goldstein, and John O. Kessler, “Fluid dynamics of self-propelled microorganisms, from individuals to concentrated populations,” *Exp. Fluids* **43**, 737–753 (2007).
4. T. Ishikawa, N. Yoshida, H. Ueno, M. Wiedeman, Y. Imai, and T. Yamaguchi, “Energy Transport in a Concentrated Suspension of Bacteria,” *Phys. Rev. Lett.* **107**, 028102 (2011).
5. Henricus H Wensink, Jörn Dunkel, Sebastian Heidenreich, Knut Drescher, Raymond E Goldstein, Hartmut Löwen, and Julia M Yeomans, “Meso-scale turbulence in living fluids,” *Proc. Natl. Acad. Sci. U. S. A.* **109**, 14308–13 (2012).
6. Jörn Dunkel, Sebastian Heidenreich, Knut Drescher, Henricus H. Wensink, Markus Bär, and Raymond E. Goldstein, “Fluid Dynamics of Bacterial Turbulence,” *Phys. Rev. Lett.* **110**, 228102 (2013).
7. Alison E. Patteson, Arvind Gopinath, and Paulo E. Arratia, “The propagation of active-passive interfaces in bacterial swarms,” *Nat. Commun.* **9**, 5373 (2018).
8. He Li, Xia-Qing Shi, Mingji Huang, Xiao Chen, Minfeng Xiao, Chenli Liu, Hugues Chaté, and H P Zhang, “Data-driven quantitative modeling of bacterial active nematics,” *Proc. Natl. Acad. Sci. U. S. A.* **116**, 777–785 (2019).
9. Yi Peng, Zhengyang Liu, and Xiang Cheng, “Imaging the emergence of bacterial turbulence: Phase diagram and transition kinetics,” *Sci. Adv.* **7**, eabd1240 (2021).
10. Zhengyang Liu, Wei Zeng, Xiaolei Ma, and Xiang Cheng, “Density fluctuations and energy spectra of 3D bacterial suspensions,” *Soft Matter* **17**, 10806–10817 (2021).
11. Da Wei, Yaochen Yang, Xuefeng Wei, Ramin Golestanian, Ming Li, Fanlong Meng, and Yi Peng, “Scaling transition of active turbulence from two to three dimensions,” (2023), [arXiv:2307.15720](https://arxiv.org/abs/2307.15720).
12. Adama Creppy, Olivier Praud, Xavier Druart, Philippa L. Kohnke, and Franck Plouraboué, “Turbulence of swarming sperm,” *Phys. Rev. E* **92**, 032722 (2015).
13. Tim Sanchez, Daniel T N Chen, Stephen J DeCamp, Michael Heymann, and Zvonimir Dogic, “Spontaneous motion in hierarchically assembled active matter,” *Nature* **491**, 431–434 (2012).
14. G. Henkin, S. J. DeCamp, D. T. N. Chen, T. Sanchez, and Z. Dogic, “Tunable dynamics of microtubule-based active isotropic gels,” *Philos. Trans. R. Soc. A Math. Phys. Eng. Sci.* **372**, 20140142 (2014).
15. Pau Guillamat, Jordi Ignés-Mullol, and Francesc Sagués, “Taming active turbulence with patterned soft interfaces,” *Nat. Commun.* **8**, 564 (2017).
16. Perry W. Ellis, Daniel J. G. Pearce, Ya-Wen Chang, Guillermo Goldsztein, Luca Giomi, and Alberto Fernandez-Nieves, “Curvature-induced defect unbinding and dynamics in active nematic toroids,” *Nat. Phys.* **14**, 85–90 (2018).
17. Nitin Kumar, Rui Zhang, Juan J. de Pablo, and Margaret L. Gardel, “Tunable structure and dynamics of active liquid crystals,” *Sci. Adv.* **4**, eaat7779 (2018).
18. Linnea M. Lemma, Stephen J. DeCamp, Zhihong You, Luca Giomi, and Zvonimir Dogic, “Statistical properties of autonomous flows in 2D active nematics,” *Soft Matter* **15**, 3264–3272 (2019).
19. Berta Martínez-Prat, Jordi Ignés-Mullol, Jaume Casademunt, and Francesc Sagués, “Selection mechanism at the onset of active turbulence,” *Nat. Phys.* **15**, 362–366 (2019).
20. Amanda J. Tan, Eric Roberts, Spencer A. Smith, Ulyses Alvarado Olvera, Jorge Arteaga, Sam Fortini, Kevin A. Mitchell, and Linda S. Hirst, “Topological chaos in active nematics,” *Nat. Phys.* **15**, 1033–1039 (2019).
21. Guillaume Duclos, Raymond Adkins, Debarghya Banerjee, Matthew S. E. Peterson, Minu Varghese, Itamar Kolvin, Arvind Baskaran, Robert A. Pelcovits, Thomas R. Powers, Aparna Baskaran, Federico Toschi, Michael F. Hagan, Sebastian J. Streichan, Vincenzo Vitelli, Daniel A. Beller, and Zvonimir Dogic, “Topological structure and dynamics of three-dimensional active nematics,” *Science* **367**, 1120–1124 (2020).
22. Berta Martínez-Prat, Ricard Alert, Fanlong Meng, Jordi Ignés-Mullol, Jean-François Joanny, Jaume Casademunt, Ramin Golestanian, and Francesc Sagués, “Scaling Regimes of Active Turbulence with External Dissipation,” *Phys. Rev. X* **11**, 031065 (2021).
23. Amin Doostmohammadi, Sumesh P Thampi, Thuan B Saw, Chwee T Lim, Benoit Ladoux, and Julia M Yeomans, “Cell division: a source of active stress in cellular monolayers,” *Soft Matter* **11**, 7328–7336 (2015).
24. Taeseok Daniel Yang, Hyun Kim, Changhyeong Yoon, Seung-Kuk Baek, and Kyoung J Lee, “Collective pulsatile expansion and swirls in proliferating tumor tissue,” *New J. Phys.* **18**, 103032 (2016).
25. C. Blanch-Mercader, V. Yashunsky, S. Garcia, G. Duclos, L. Giomi, and P. Silberzan, “Turbulent Dynamics of Epithelial Cell Cultures,” *Phys. Rev. Lett.* **120**, 208101 (2018).
26. Shao-Zhen Lin, Wu-Yang Zhang, Dapeng Bi, Bo Li, and Xi-Qiao Feng, “Energetics of mesoscale cell turbulence in two-dimensional monolayers,” *Commun. Phys.* **4**, 21 (2021).
27. Xin Li, Sumit Sinha, T. R. Kirkpatrick, and D. Thirumalai, “Topological transitions, turbulent-like motion and long-time tails driven by cell division in biological tissues,” (2022), [arXiv:2211.14410](https://arxiv.org/abs/2211.14410).
28. Daiki Nishiguchi and Masaki Sano, “Mesoscopic turbulence and local order in Janus particles self-propelling under an ac electric field,” *Phys. Rev. E* **92**, 052309 (2015).
29. Gašper Kokot, Shibananda Das, Roland G Winkler, Gerhard Gompper, Igor S Aranson, and Alexey Snezhko, “Active turbulence in a gas of self-assembled spinners,” *Proc. Natl. Acad. Sci. U. S. A.* **114**, 12870–12875 (2017).
30. Hamid Karani, Gerardo E. Pradillo, and Petia M. Vlahovska,

- “Tuning the Random Walk of Active Colloids: From Individual Run-and-Tumble to Dynamic Clustering,” *Phys. Rev. Lett.* **123**, 208002 (2019).
31. Mickael Bourgoin, Ronan Kervil, Cecile Cottin-Bizonne, Florence Raynal, Romain Volk, and Christophe Ybert, “Kolmogorovian Active Turbulence of a Sparse Assembly of Interacting Marangoni Surfers,” *Phys. Rev. X* **10**, 021065 (2020).
  32. Luca Giomi, “Geometry and Topology of Turbulence in Active Nematics,” *Phys. Rev. X* **5**, 031003 (2015).
  33. Ricard Alert, Jean-François Joanny, and Jaume Casademunt, “Universal scaling of active nematic turbulence,” *Nat. Phys.* **16**, 682–688 (2020).
  34. Amin Doostmohammadi, Jordi Ignés-Mullol, Julia M. Yeomans, and Francesc Sagués, “Active nematics,” *Nat. Commun.* **9**, 3246 (2018).
  35. Pierre-Gilles de Gennes and Jacques Prost, *The Physics of Liquid Crystals*, 2nd ed. (Oxford University Press, New York, 1993).
  36. Frank Jülicher, Stephan W Grill, and Guillaume Salbreux, “Hydrodynamic theory of active matter,” *Reports Prog. Phys.* **81**, 076601 (2018).
  37. Ido Lavi, Ricard Alert, Jean-François Joanny, and Jaume Casademunt, “Nonlinear spontaneous flow instability in active nematics,” *arXiv preprint arXiv:2403.16841* (2024).
  38. K Kruse, J F Joanny, F. Jülicher, J Prost, and K Sekimoto, “Generic theory of active polar gels: a paradigm for cytoskeletal dynamics,” *Eur. Phys. J. E* **16**, 5–16 (2005).
  39. M. C. Marchetti, J. F. Joanny, S. Ramaswamy, T. B. Liverpool, J. Prost, Madan Rao, and R. Aditi Simha, “Hydrodynamics of soft active matter,” *Rev. Mod. Phys.* **85**, 1143–1189 (2013).
  40. J. Prost, F. Jülicher, and J-F. Joanny, “Active gel physics,” *Nat. Phys.* **11**, 111–117 (2015).
  41. S. A. Edwards and J. M. Yeomans, “Spontaneous flow states in active nematics: A unified picture,” *Europhys. Lett.* **85**, 18008 (2009).
  42. Luca Giomi, Mark J Bowick, Prashant Mishra, Rastko Sknepnek, and M. Cristina Marchetti, “Defect dynamics in active nematics,” *Philos. Trans. A. Math. Phys. Eng. Sci.* **372**, 20130365 (2014).
  43. Sumesh P. Thampi, Ramin Golestanian, and Julia M. Yeomans, “Instabilities and topological defects in active nematics,” *Europhys. Lett.* **105**, 18001 (2014).
  44. Sumesh P Thampi, Ramin Golestanian, and Julia M Yeomans, “Vorticity, defects and correlations in active turbulence,” *Philos. Trans. R. Soc. A Math. Phys. Eng. Sci.* **372**, 20130366 (2014).
  45. S.P. Thampi and J.M. Yeomans, “Active turbulence in active nematics,” *Eur. Phys. J. Spec. Top.* **225**, 651–662 (2016).
  46. R Voituriez, J F Joanny, and J Prost, “Spontaneous flow transition in active polar gels,” *Europhys. Lett.* **70**, 404–410 (2005).
  47. Rajesh Ramaswamy and Frank Jülicher, “Activity induces traveling waves, vortices and spatiotemporal chaos in a model actomyosin layer,” *Scientific reports* **6**, 20838 (2016).
  48. P. A. M. Dirac, “Quantised Singularities in the Electromagnetic Field,” *Proc. R. Soc. A Math. Phys. Eng. Sci.* **133**, 60–72 (1931).
  49. Pooja Chandrakar, Minu Varghese, S.Ali Aghvami, Aparna Baskaran, Zvonimir Dogic, and Guillaume Duclos, “Confinement Controls the Bend Instability of Three-Dimensional Active Liquid Crystals,” *Phys. Rev. Lett.* **125**, 257801 (2020).
  50. Pau Guillamat, Jordi Ignés-Mullol, and Francesc Sagués, “Control of active liquid crystals with a magnetic field,” *Proc. Natl. Acad. Sci.* **113**, 5498–5502 (2016).
  51. Stephen J DeCamp, Gabriel S Redner, Aparna Baskaran, Michael F Hagan, and Zvonimir Dogic, “Orientational order of motile defects in active nematics,” *Nature materials* **14**, 1110–1115 (2015).
  52. Linnea M. Lemma, Michael M. Norton, Alexandra M. Tayar, Stephen J. DeCamp, S. Ali Aghvami, Seth Fraden, Michael F. Hagan, and Zvonimir Dogic, “Multiscale Microtubule Dynamics in Active Nematics,” *Phys. Rev. Lett.* **127**, 148001 (2021).
  53. Bo Li, Kai Lou, Walter Kob, and Steve Granick, “Anatomy of cage formation in a two-dimensional glass-forming liquid,” *Nature* **587**, 225–229 (2020).
  54. C. Patrick Royall, Stephen R. Williams, Takehiro Ohtsuka, and Hajime Tanaka, “Direct observation of a local structural mechanism for dynamic arrest,” *Nat. Mater.* **7**, 556–561 (2008).
  55. C. Patrick Royall and Stephen R. Williams, “The role of local structure in dynamical arrest,” *Phys. Rep.* **560**, 1–75 (2015).
  56. Jennifer Billock, “Walk the world’s most meditative labyrinths,” *Smithsonian Magazine* (2016).
  57. I. Bordeu, M. G. Clerc, R. Lefever, and M. Tlidi, “From localized spots to the formation of invaginated labyrinthine structures in a Swift-Hohenberg model,” *Commun. Nonlinear Sci. Numer. Simul.* **29**, 482–487 (2015).
  58. M Seul, L R Monar, L O Gorman, and R Wolfe, “Morphology and Local Structure in Labyrinthine Stripe Domain Phase,” *Science* **254**, 1616–1618 (1991).
  59. M. Seul, L. R. Monar, and L. O’Gorman, “Pattern analysis of magnetic stripe domains morphology and topological defects in the disordered state,” *Philos. Mag. B* **66**, 471–506 (1992).
  60. Bert Reimann, Reinhard Richter, and Ingo Rehberg, “Glasslike relaxation of labyrinthine domain patterns,” *Phys. Rev. E* **65**, 031504 (2002).
  61. Martin James, Wouter JT Bos, and Michael Wilczek, “Turbulence and turbulent pattern formation in a minimal model for active fluids,” *Physical Review Fluids* **3**, 061101 (2018).
  62. Xander M de Wit, Michel Fruchart, Tali Khain, Federico Toschi, and Vincenzo Vitelli, “Pattern formation by turbulent cascades,” *Nature* **627**, 515–521 (2024).
  63. Haoran Xu and Yilin Wu, “Self-enhanced mobility enables vortex pattern formation in living matter,” *Nature* **627**, 553–558 (2024).
  64. RF Wang, C Nisoli, RS Freitas, J Li, W McConville, BJ Cooley, MS Lund, N Samarth, C Leighton, VH Crespi, and P Schiffer, “Artificial ‘spin ice’ in a geometrically frustrated lattice of nanoscale ferromagnetic islands,” *Nature* **439**, 303–306 (2006).
  65. Rayan Chatterjee, Navdeep Rana, R. Aditi Simha, Prasad Perlekar, and Sriram Ramaswamy, “Inertia Drives a Flocking Phase Transition in Viscous Active Fluids,” *Phys. Rev. X* **11**, 031063 (2021).
  66. Benjamin H. Andersen, Julian Renaud, Jonas Rønning, Luiza Angheluta, and Amin Doostmohammadi, “Symmetry-restoring crossover from defect-free to defect-laden turbulence in polar active matter,” *Phys. Rev. Fluids* **8**, 063101 (2023).
  67. Renato Assante, Dom Corbett, Davide Marenduzzo, and Alexander Morozov, “Active turbulence and spontaneous phase separation in inhomogeneous extensible active gels,” *Soft Matter* **19**, 189–198 (2023).
  68. F. Hecht, “New development in freefem++,” *J. Numer. Math.* **20**, 251–265 (2012).
  69. Joseph Hun Wei Lee, Jaime Peraire, and Olgierd C Zienkiewicz, “The characteristic-galerkin method for advection-dominated problems—an assessment,” *Computer methods in applied mechanics and engineering* **61**, 359–369 (1987).

## METHODS

### A. Numerical scheme

Here we describe our method for numerically integrating Eqs. (6) to (8). In what follows, the index  $n$  is the time iteration,  $dt$  is the timestep, and  $h = N^{-1}$  is the vertex spacing on our  $N \times N$  square grid.

#### 1. Solving momentum balance (pseudo-spectral method)

In each time iteration, we first solve for the streamfunction based on  $\theta^n$ , the array representing the current director angle on the vertices. After rearranging terms and substituting  $\hat{q}_{\alpha\beta}(\theta)$  and  $\bar{q}_{\alpha\beta}(\theta)$  in Eq. (6), one has

$$\begin{aligned} \nabla^4 \psi^n + G(\theta^n, \psi^n) &= S(d_1 \sin 2\theta^n + d_2 \cos 2\theta^n) \\ &- \frac{R}{A} \left( \frac{1}{2} \nabla^4 \theta^n + (\partial_x \nabla^2 \theta^n) \partial_y \theta^n - (\partial_y \nabla^2 \theta^n) \partial_x \theta^n \right. \\ &\left. + \nu (d_1 \cos 2\theta^n \nabla^2 \theta^n - d_2 \sin 2\theta^n \nabla^2 \theta^n) \right), \end{aligned} \quad (9)$$

where we defined  $d_1 := \frac{1}{2}(\partial_y^2 - \partial_x^2)$ ,  $d_2 := \partial_y \partial_x$  and

$$G(\theta, \psi) := R\nu \left( d_1 \sin 2\theta h_{\parallel}(\theta, \psi) + d_2 \cos 2\theta h_{\parallel}(\theta, \psi) \right),$$

with

$$h_{\parallel}(\theta, \psi) = \nu (\sin 2\theta d_1 \psi + \cos 2\theta d_2 \psi).$$

To find the solution  $\psi^n$  we employ a pseudo-spectral method, with all derivatives calculated in the space of the two-dimensional discrete Fourier transform (DFT) and all non-linear operations performed in real-space. Before each real-space multiplication, we apply the 2/3 de-aliasing rule, truncating the Fourier modes with  $|q_x|$  or  $|q_y|$  greater than  $\frac{2}{3}\pi N$ .

We begin by computing the right-hand side (RHS) of Eq. (9), which is independent of  $\psi^n$ . Next, we note that  $G(\theta^n, \psi^n)$ , the second term on the left-hand side (LHS) of Eq. (9), consists of non-constant coefficients combined with high-order derivatives. This defines a dense matrix in Fourier space that also varies in time. The high computation cost associated with building and inverting such a matrix at every time step renders direct inversion impractical. We therefore treat this term explicitly in a fixed-point iteration scheme, where we aim to compute a converging sequence  $\{\psi^{n_k}\}_k$  (with  $k = 0, 1, 2, \dots$ ). Given an explicit approximation  $\psi^{n_k}$ ,  $G(\theta^n, \psi^{n_k})$  is computed pseudo-spectrally and transferred to the RHS. The subsequent iteration is then obtained by keeping the biharmonic term on the LHS implicit. By inverting the modified problem in Fourier space, the  $k^{\text{th}}$  iteration is given by

$$\mathcal{F}[\psi^{n_{k+1}}] = \frac{1}{q^4} (\mathcal{F}[\text{RHS}(\theta^n)] - \mathcal{F}[G(\theta^n, \psi^{n_k})]) \quad \forall q \neq 0, \quad (10)$$

where  $\mathcal{F}[\cdot]$  indicates the DFT and  $q = \|\mathbf{q}\|$ . The mode  $q = 0$  in the streamfunction is always truncated as it has no

bearing on the flow. To aid convergence, we initiate the sequence with the solution obtained in the previous time step, i.e.  $\psi^{n_0} = \psi^{n-1}$ . Iterations on  $k$  are performed until a convergence criterion for the residual error  $\eta$  is met. Formally, we compute

$$\eta_{k+1} = \frac{\int_{\Omega} (\psi^{n_{k+1}} - \psi^{n_k})^2}{\int_{\Omega} (\psi^{n_k})^2}$$

and we check whether  $\eta_{k+1} < \epsilon$ , with  $\epsilon$  a small computational tolerance (typically  $10^{-8}$ ). While convergence is empirically tested, it is not guaranteed in the fixed-point method. With our chosen physical and numerical parameters, we find robust convergence so long as  $|\nu| \lesssim 1.5$ .

#### 2. Computing the flow, vorticity and flow-alignment rotations

After obtaining a convergent streamfunction  $\psi^n$ , and before attending to Eq. (8), we compute the following fields pseudo-spectrally:

$$\begin{aligned} v_x^n &= \partial_y \psi^n, \quad v_y^n = -\partial_x \psi^n, \quad \omega^n = -\nabla^2 \psi^n, \\ C^n &= -\hat{q}_{\alpha\beta}(\theta^n) \partial_{\alpha} \partial_{\beta} \psi^n = \cos 2\theta^n d_1 \psi^n - \sin 2\theta^n d_2 \psi^n. \end{aligned} \quad (11)$$

Respectively, these represent arrays of the flow components, vorticity, and a term proportional to flow alignment rotations ( $C^n$ ), defined on the vertices of the  $N \times N$  grid.

#### 3. Evolving the angle field (finite element method)

We chose to evolve Eq. (8) with the finite-element method (FEM), using the open source package FreeFem++<sup>68</sup>. The nodes of our triangular mesh  $\mathcal{T}_h$ , spanning the square domain  $\Omega$ , coincide with the regular grid points. With this arrangement, it is straightforward to map the data  $v_{\alpha}^n$ ,  $\omega^n$ , and  $C^n$  (Eq. (11)) to the amplitudes of linear finite-element ‘hat functions’.

To ensure stability of the scheme, we first tackle the convective term in Eq. (8) independently via the Characteristics-Galerkin method<sup>69</sup>. Specifically, we solve the hyperbolic problem  $\partial_t \theta + \mathbf{v} \cdot \nabla \theta = 0$  with the built-in **convect** function<sup>68</sup>:  $\theta_{\text{adv}}^n = \text{convect}(\mathbf{v}^n, -dt, \theta^n)$ .

Next, we formulate the time-discretized version of the rotations prescribed by Eq. (8),

$$(\theta^{n+1} - \theta_{\text{adv}}^n)/dt - \frac{1}{2} \omega^n = \frac{1}{A} \nabla^2 \theta^{n+1} - \nu C^n, \quad (12)$$

where we opted to handle the Laplacian term implicitly for enhanced stability.

To proceed with FEM, we write the weak form of Eq. (12),

$$\begin{aligned} \int_{\Omega} \theta^{n+1} \phi \, d^2 \mathbf{r} + \frac{dt}{A} \int_{\Omega} \nabla \theta^{n+1} \cdot \nabla \phi \, d^2 \mathbf{r} = \\ \int_{\Omega} \theta_{\text{adv}}^n \phi \, d^2 \mathbf{r} + \frac{dt}{2} \int_{\Omega} \omega^n \phi \, d^2 \mathbf{r} - dt \nu \int_{\Omega} C^n \phi \, d^2 \mathbf{r}. \end{aligned} \quad (13)$$

The problem consists in finding a solution  $\theta^{n+1} \in H^1(\Omega)$  for any arbitrary smooth test function  $\phi : \Omega \rightarrow \mathbb{R}$ .

The terms on the LHS of Eq. (13) are bilinear (implicit) while those on the RHS are linear (explicit). In our code,  $\theta$  and  $\phi$  are represented by the basis functions spanning the continuous **P2** finite-element space, i.e., polynomials of degree 2 defined piecewise on each element  $K \in \mathcal{T}_h$ . By imposing doubly-periodic boundary conditions, the boundary term coming from integration by parts vanishes. The matrix defined by the LHS is inverted using the default **sparsecv** in FreeFem++<sup>68</sup>.

#### 4. Adding noise

To speed up the evolution towards fully-developed active turbulence, we introduce small-amplitude stochastic fluctuations to  $\partial_t \theta$  in the spirit of previous work<sup>33</sup>. We use a Gaussian white noise field  $\xi(\mathbf{r}, t)$  with zero mean and uncorrelated in both space and time, i.e.  $\langle \xi(\mathbf{r}, t) \rangle = 0$  and  $\langle \xi(\mathbf{r}, t) \xi(\mathbf{r}', t') \rangle = 2D \delta(\mathbf{r} - \mathbf{r}') \delta(t - t')$ .

In more detail, we define  $\xi^n$  (the noise array at time  $dt n$ ) in Fourier space by assigning to each mode a Gaussian random amplitude  $a_{\mathbf{q}}$  and a random phase  $\phi_{\mathbf{q}}$ , expressed as  $a_{\mathbf{q}} e^{i\phi_{\mathbf{q}}}$ . The zero mode is truncated to impose a zero mean. To further counter aliasing, we also truncate the highest wave-numbers for which  $|q_x|$  or  $|q_y|$  are greater than  $\frac{2}{3}\pi N$ . After taking the real part of the inverse DFT, the resulting noise is scaled by  $\frac{\sqrt{3D}}{\sqrt{dth^2}}$ . This factor ensures that the fluctuations are properly normalized, taking into account the space and time discretizations, as well as the 2/3 filtering. The normalized noise  $\xi^n$  is added to the RHS of Eq. (12), resulting in an explicit integral term in the weak formulation, Eq. (13).

We verified that spatio-temporal chaos persists also in the absence of noise. Additionally, we found that increasing the noise amplitude enhances the velocity fluctuations, especially at large scales, thereby expanding the  $q^{-1}$  scaling region.

#### 5. Additional notes

- The triangular FEM mesh  $\mathcal{T}_h$  spans the entire periodic domain, resulting in  $(N + 1) \times (N + 1)$  nodes. Thus, before proceeding to stage 3, we extend the real-space  $N \times N$  arrays (Eq. (11) and the noise  $\xi^n$ ) so that the added data along the  $x = 1$  and  $y = 1$  edges matches the data along the  $x = 0$  and  $y = 0$  edges, respectively.
- To allow the pseudo-spectral computations involved in stage 1, the data stored in the **P2** finite-element representation of  $\theta^n$  is first downgraded to a **P1** representation to obtain the field values on the  $N \times N$  vertices.

#### 6. Numerical parameters

In the large-scale simulations (Figs. 1 and 5, Supplementary Fig. 1 and Movies 1–3, 5) we fixed  $N = 256$ ,  $dt = 0.01$ , and

$D = 0.0025^2$ . In the simulations depicted in Fig. 2, Supplementary Movie 4, we fixed  $N = 128$ ,  $dt = 0.02$ , and  $D = 0$  (zero noise).

### 7. Verification

We verified our computational solver for different parameter values. As demonstrated in Supplementary Fig. 6, we compare the numerical output against two criteria: (i) long-time relaxation to predicted one-dimensional steady states (nonlinear striped patterns) that are stable at moderate activity levels<sup>33,37</sup> (Supplementary Fig. 6b), and (ii) the linear growth rate of small Fourier perturbations around the uniformly aligned quiescent state<sup>33,37</sup> (Supplementary Fig. 6c).

### B. Spectra

Here we detail the computation of the spectra presented in Figs. 1g to 1i and Supplementary Fig. 2. In the equations below we use the following notations:

- $\tilde{f}(\mathbf{q})$  is the two-dimensional DFT of  $f(\mathbf{r})$ , i.e.  $\tilde{f} = \mathcal{F}[f]$ .
- $\langle f(\mathbf{r}) \rangle_{\mathbf{r}}$  is the spatial average of  $f(\mathbf{r})$  over  $\Omega$ .
- $\langle \tilde{f}(\mathbf{q}) \rangle_{\phi}$  is the mean of all  $\tilde{f}(\mathbf{q})$  for which  $\mathbf{q} = q(\cos \phi, \sin \phi)$ , i.e. an azimuthal average in Fourier space.
- $\langle \cdot \rangle$  is an ensemble average within fully developed active turbulence. In our long simulations, this is practically computed as the temporal mean for  $t > t_T$ , with  $t_T$  the onset time of a statistical steady state. To preclude initial transients, we empirically set  $t_T = 200\tau_a$  ( $2 \times 10^4$  computational time iterations).

#### 1. Velocity power spectrum

The velocity power spectrum in the 2D Fourier space is defined by<sup>33</sup>

$$E(\mathbf{q}) = \frac{1}{2} \langle \tilde{v}_{\alpha}^*(\mathbf{q}) \tilde{v}_{\alpha}(\mathbf{q}) \rangle = \frac{1}{2} q^2 \left\langle \left| \tilde{\psi}(\mathbf{q}) \right|^2 \right\rangle. \quad (14)$$

Under the assumption of statistical isotropy, one has

$$E(q) = 2\pi q \langle E(\mathbf{q}) \rangle_{\phi} = \pi q^3 \left\langle \left\langle \left| \tilde{\psi}(\mathbf{q}) \right|^2 \right\rangle \right\rangle_{\phi}. \quad (15)$$

Since  $\mathbf{v}$  is in units of  $[L/\tau_a]$  and  $q$  is in units of  $[L^{-1}]$ ,  $E(q)$  is given in units of  $[L/\tau_a^2]$  (Fig. 1g).

## 2. Frank energy spectrum

The Frank energy spectrum (or  $\nabla\theta$  power spectrum) is defined by<sup>33</sup>

$$F_n(\mathbf{q}) = \frac{K}{2} \langle \mathcal{F}[\partial_\alpha \theta]^*(\mathbf{q}) \mathcal{F}[\partial_\alpha \theta](\mathbf{q}) \rangle = \frac{K}{2} q^2 \left\langle \left| \tilde{\theta}(\mathbf{q}) \right|^2 \right\rangle. \quad (16)$$

Under the assumption of statistical isotropy,

$$F_n(q) = 2\pi q \langle F_n(\mathbf{q}) \rangle_\phi = \pi K q^3 \left\langle \left\langle \left| \tilde{\theta}(\mathbf{q}) \right|^2 \right\rangle \right\rangle_\phi. \quad (17)$$

Because  $q$  is in units of  $[L^{-1}]$ ,  $F_n(\mathbf{q})$  is given in units of  $[K/L^3]$  (Fig. 1h).

## 3. Correlation time spectra

The nematic order parameter in our case, with the scalar amplitude fixed to 1, is the tensor  $\hat{q}_{\alpha\beta} = n_\alpha n_\beta - 1/2 \delta_{\alpha\beta}$  (not be confused with the wavevector  $\mathbf{q}$ ). In terms of  $\theta$ ,

$$\hat{q} = \frac{1}{2} \begin{pmatrix} \cos 2\theta & \sin 2\theta \\ \sin 2\theta & -\cos 2\theta \end{pmatrix}. \quad (18)$$

We define  $\mathcal{C}_{\hat{q}\hat{q}}(\mathbf{x}, \tau)$  as the space-time autocorrelation function of  $\hat{q}$ ,

$$\mathcal{C}_{\hat{q}\hat{q}}(\mathbf{x}, \tau) = \langle \langle \hat{q}_{\alpha\beta}(\mathbf{r}, t) \hat{q}_{\alpha\beta}(\mathbf{r} + \mathbf{x}, t + \tau) \rangle \rangle_{\mathbf{r}}, \quad (19)$$

where  $\mathbf{x}$  is the two point vector and  $\tau$  is the lag time. For a given  $\tau$ , the frames considered in the time average correspond to  $t_T \leq t \leq T - \tau$ , with  $T$  the total runtime of the simulation.

The spatial Fourier transform of  $\mathcal{C}_{\hat{q}\hat{q}}$  is then

$$\begin{aligned} \tilde{\mathcal{C}}_{\hat{q}\hat{q}}(\mathbf{q}, \tau) &= \langle \mathcal{F}[\hat{q}_{\alpha\beta}]^*(\mathbf{q}, t) \mathcal{F}[\hat{q}_{\alpha\beta}](\mathbf{q}, t + \tau) \rangle \quad (20) \\ &= \frac{1}{2} \langle \mathcal{F}[\cos 2\theta]^*(\mathbf{q}, t) \mathcal{F}[\cos 2\theta](\mathbf{q}, t + \tau) \rangle \\ &\quad + \frac{1}{2} \langle \mathcal{F}[\sin 2\theta]^*(\mathbf{q}, t) \mathcal{F}[\sin 2\theta](\mathbf{q}, t + \tau) \rangle. \end{aligned}$$

For each mode  $\mathbf{q}$ , we fit the time series  $\tilde{\mathcal{C}}_{\hat{q}\hat{q}}(\mathbf{q}, \tau)$  to an exponential  $\tilde{\mathcal{C}}_{\hat{q}\hat{q}}(\mathbf{q}, 0)e^{-\tau/\tau_{\hat{q}}}$ , with  $\tau_{\hat{q}}$  the fitting parameter, using the **NonlinearModelFit** function in Mathematica (TM). This fitting gives  $\tau_{\hat{q}}(\mathbf{q})$ . The azimuthal average  $\tau_{\hat{q}}(q) = \langle \tau_{\hat{q}}(\mathbf{q}) \rangle_\phi$  is shown in Fig. 1i (dark data points).

Next, we define the space-time autocorrelation function of the flow  $\mathbf{v}$ :

$$\mathcal{C}_{\mathbf{v}\mathbf{v}}(\mathbf{x}, \tau) = \langle \langle v_\alpha(\mathbf{r}, t) v_\alpha(\mathbf{r} + \mathbf{x}, t + \tau) \rangle \rangle_{\mathbf{r}} \quad (21)$$

The spatial Fourier transform of  $\mathcal{C}_{\mathbf{v}\mathbf{v}}$  is given by

$$\begin{aligned} \tilde{\mathcal{C}}_{\mathbf{v}\mathbf{v}}(\mathbf{q}, \tau) &= \langle \tilde{v}_\alpha^*(\mathbf{q}, t) \tilde{v}_\alpha(\mathbf{q}, t + \tau) \rangle \quad (22) \\ &= q^2 \langle \tilde{\psi}^*(\mathbf{q}, t) \tilde{\psi}(\mathbf{q}, t + \tau) \rangle. \end{aligned}$$

Note that  $E(\mathbf{q}) = \frac{1}{2} \tilde{\mathcal{C}}_{\mathbf{v}\mathbf{v}}(\mathbf{q}, \tau = 0)$  (see Eq. (14)).

For each mode  $\mathbf{q}$ , we fit the time series  $\tilde{\mathcal{C}}_{\mathbf{v}\mathbf{v}}(\mathbf{q}, \tau)$  to an exponential  $\tilde{\mathcal{C}}_{\mathbf{v}\mathbf{v}}(\mathbf{q}, 0)e^{-\tau/\tau_{\mathbf{v}}}$ , with  $\tau_{\mathbf{v}}$  the fitting parameter. This fitting gives  $\tau_{\mathbf{v}}(\mathbf{q})$ . The azimuthal average  $\tau_{\mathbf{v}}(q) = \langle \tau_{\mathbf{v}}(\mathbf{q}) \rangle_\phi$  is shown in Fig. 1i (light data points).

## 4. Nematic tensor power spectrum

The nematic tensor power spectrum is defined by

$$W(\mathbf{q}) = \langle \mathcal{F}[\hat{q}_{\alpha\beta}]^*(\mathbf{q}) \mathcal{F}[\hat{q}_{\alpha\beta}](\mathbf{q}) \rangle. \quad (23)$$

By this definition, one has  $W(\mathbf{q}) = \tilde{\mathcal{C}}_{\hat{q}\hat{q}}(\mathbf{q}, \tau = 0)$  (see Eq. (20)).

Under the assumption of statistical isotropy,

$$\begin{aligned} W(q) &= 2\pi q \langle W(\mathbf{q}) \rangle_\phi \quad (24) \\ &= \pi q \langle \langle \mathcal{F}[\cos 2\theta]^*(\mathbf{q}) \mathcal{F}[\cos 2\theta](\mathbf{q}) \rangle \rangle_\phi \\ &\quad + \langle \mathcal{F}[\sin 2\theta]^*(\mathbf{q}) \mathcal{F}[\sin 2\theta](\mathbf{q}) \rangle \rangle_\phi. \end{aligned}$$

Since  $\hat{q}$  is dimensionless and  $q$  is in units of  $[L^{-1}]$ ,  $W(\mathbf{q})$  is given in units  $[L^{-1}]$  (Supplementary Fig. 2).

## C. Image processing

### 1. Skeleton detection and pseudo-defect classification

The process of skeleton detection and pseudo-defect classification is depicted in Supplementary Fig. 4. We apply the following pipeline using the image processing tools in Mathematica (TM).

Initially, a plot of the Frank free energy density,  $|\nabla\theta|^2$ , is rendered (Supplementary Fig. 4a). The grayscale color scheme and the plot range are chosen to aid the binarization of the walls. To avoid false node detection along the square boundaries, this plot is periodically expanded using the **ImageAssemble** function (Supplementary Fig. 4b). Subsequently, we binarize the image by applying the **LocalAdaptiveBinarize** function, with neighbourhood pixel range set to 6. Then, we apply the **DeleteSmallComponents** function to remove isolated white domains, specified as totalling 20 or fewer pixels, that we do not consider part of the wall network (Supplementary Fig. 4c).

To obtain the network skeleton, we apply the **Thinning** function with default setting on the binarized image. At times, this alone can leave tiny black gaps within some walls that would later be falsely interpreted as branching points. To avoid this, we further apply the **Dilation** function, with range set to 1 pixel, and then repeat **Thinning**. To prune short branches from the skeleton we apply the **Pruning** function, specifying the range to 2 pixels. The final skeleton is shown in Supplementary Fig. 4d.

The nodes of the skeleton are then detected using the **MorphologicalTransform** function, specifying "SkeletonBranchPoints" and then "SkeletonEndPoints" (highlighted in blue and red respectively in Supplementary Fig. 4e). The nodes are filtered to retain only those within the original square (Supplementary Fig. 4f). At this stage, the "SkeletonBranchPoints" correspond to our pseudo-defect branchpoints (Fig. 3b). However, the "SkeletonEndPoints" can be either pseudo-defect endpoints (Fig. 3c) or startpoints (Fig. 3a).

To distinguish between endpoints and startpoints, we test whether the wall polarity faces outwards or inwards with respect to the branch associated with each "SkeletonEndPoint". To this end, we compute two vectors on each such node. The vector pointing outwards from the associated branch is calculated by locating the nearest neighboring point on the wall skeleton (Supplementary Fig. 4g). The wall polarity at each node is determined by  $(\partial_y \theta, -\partial_x \theta)$ . The scalar product of the polarity with the outwards vector classifies the type of pseudo-defect (Supplementary Fig. 4h).

Finally, Supplementary Fig. 4i displays the classified nodes with branchpoints (blue), endpoints (red), and startpoints (green)—all oriented according to the local wall polarity.

## 2. Labyrinths detection

The process of labyrinth detection in arrested wall networks is depicted in Supplementary Fig. 5. Here, the frames of interest are those in which no startpoints have been detected. Similarly to our skeleton detection scheme, we apply a pipeline

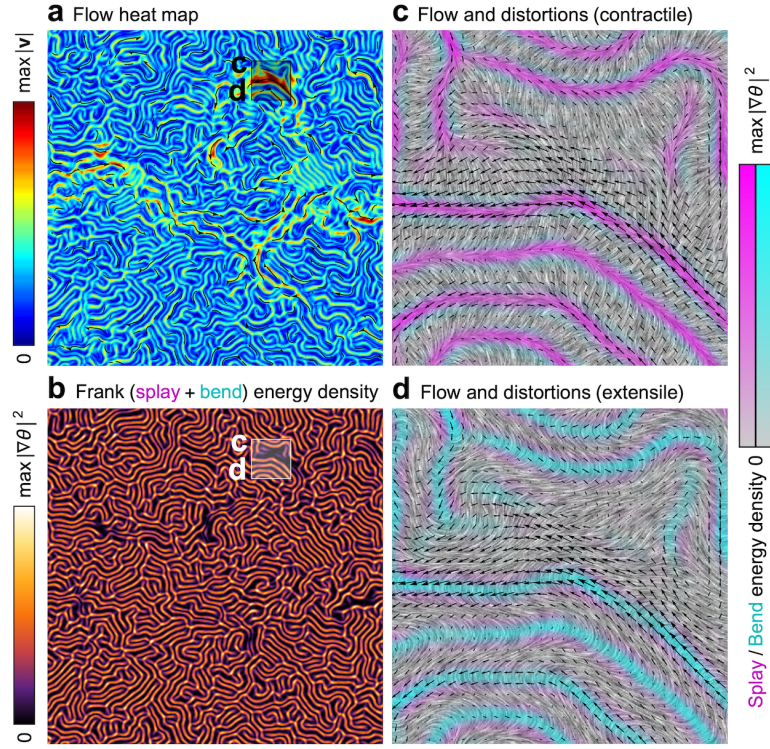
that uses the image processing tools in Mathematica (TM).

Initially, an inverted plot of  $|\nabla \theta|^2$  is rendered (Supplementary Fig. 5a). The color scheme and plot range are selected to aid the binarization of the gaps between the walls. To assist in identifying connected domains that frequently pass through the square boundaries, this plot is periodically expanded using the **ImageAssemble** function (Supplementary Fig. 5b). The **LocalAdaptiveBinarize** function is then applied with a neighborhood pixel range set to 10, followed by the **FillingTransform** function to eliminate isolated black fragments not considered as walls (Supplementary Fig. 5c).

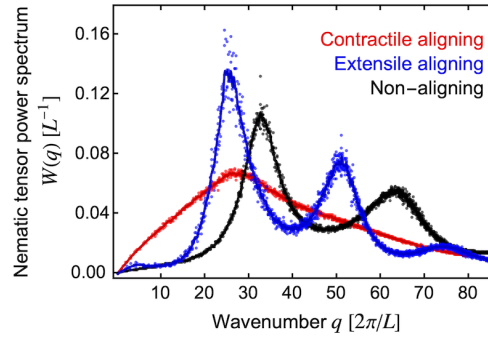
Next, we find the connected morphological domains in the binarized image using the **MorphologicalComponents** function (Supplementary Fig. 5d). These distinctly labeled domains are then cropped to retain only those within the original periodic square (Supplementary Fig. 5e).

To relabel domains that connect through the left-right and top-bottom boundaries, we employ a custom algorithm that ensures continuity across the periodic square (Supplementary Fig. 5f). This step completes the process of detecting the unicursal labyrinths which span the system size.

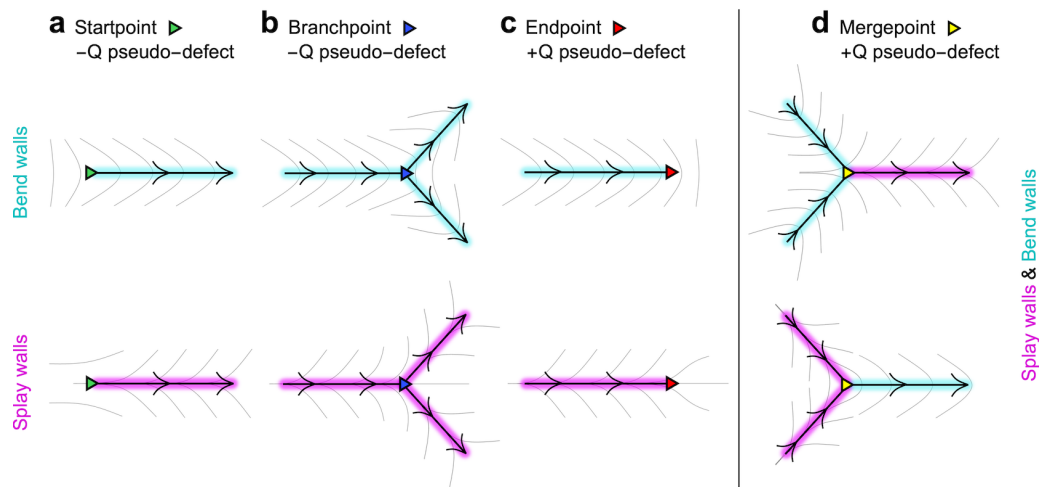
## SUPPLEMENTARY FIGURES



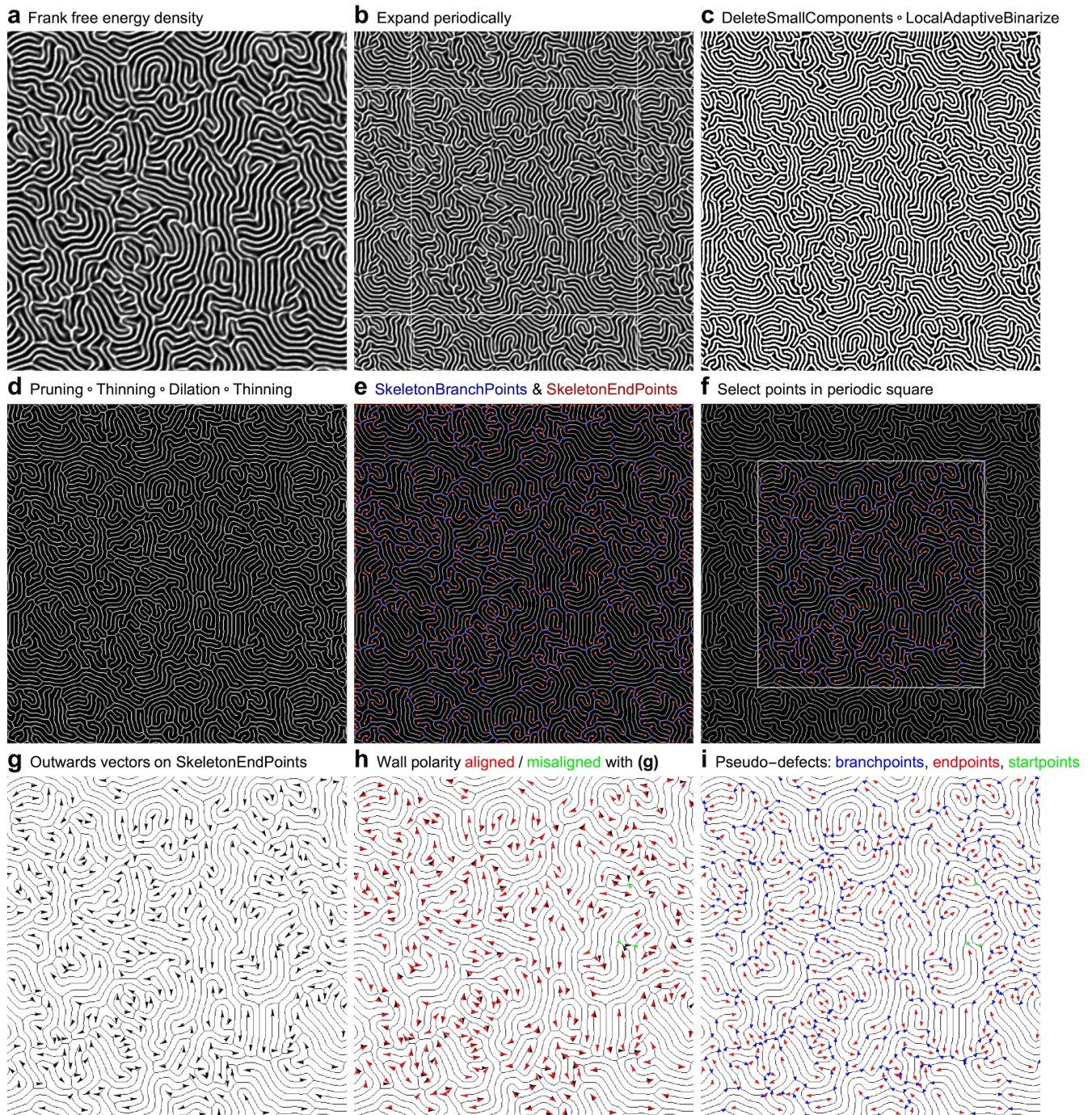
**Supplementary Figure 1 | Active nematic turbulence in the absence of flow-alignment.** Snapshots from a simulation of defect-free active nematic turbulence with parameter values  $R = 1$ ,  $\nu = 0$ , and  $A = 3.2 \times 10^5$ . We chose a contractile stress ( $S = -1$ ), but the results are exactly equivalent in the extensile case ( $S = +1$ ) when the director is rotated ( $\theta \rightarrow \theta \pm \pi/2$ ). **a**, The flow field; black curves are streamlines, and the color indicates the speed (Supplementary Movie 3, left). **b**, Frank free energy density  $\sim |\nabla\theta|^2$ , with high-intensity lines corresponding to nematic domain walls (Supplementary Movie 3, right). Note how sparse peaks in the flow (red regions in **a**) tend to coincide with perturbed wall patterns (dark regions in **b**). **c-d**, Zooms in the contractile (**c**) and extensile (**d**) cases highlighting the type of nematic distortion as well as the interplay between nematic walls and flows. The gray-scale background is the line integral convolution representation of the director field  $\mathbf{n}$ . Magenta and cyan intensities respectively represent splay  $(\nabla \cdot \mathbf{n})^2$  and bend  $|\nabla \times \mathbf{n}|^2$  contributions to the Frank energy density. The black arrows represent the flow field  $\mathbf{v}$ .



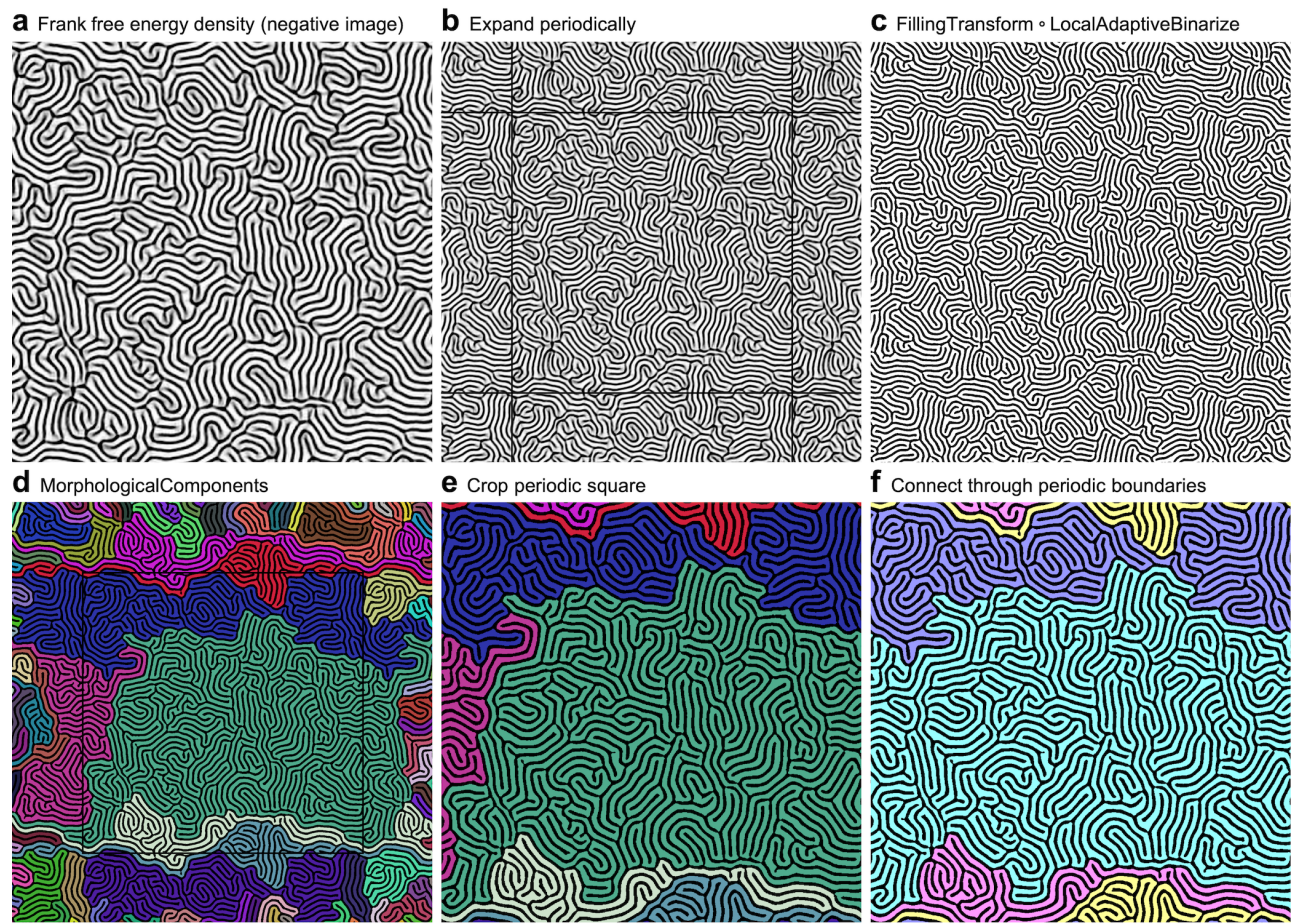
**Supplementary Figure 2 | Power spectrum of the order parameter in active nematic turbulence.** Shown is the power spectrum of the nematic tensor,  $\hat{q}_{\alpha\beta} = n_\alpha n_\beta - 1/2 \delta_{\alpha\beta}$ , in the contractile flow-aligning ( $S\nu = +1.1$ , red), extensile flow-aligning ( $S\nu = -1.1$ , blue), and non-aligning ( $\nu = 0$ , black) cases. For the definition of  $W(q)$  see Methods B. Lines represent a smoothed (Gaussian) interpolation of the computed data points. Parameter values are as in Fig. 1 and Supplementary Fig. 1. For arrested turbulence (blue), this spectrum features a narrow peak with its associated harmonics. For strong large-scale turbulence (red), such peaks are washed out. In all regimes, low- $q$  correlations are essentially absent.



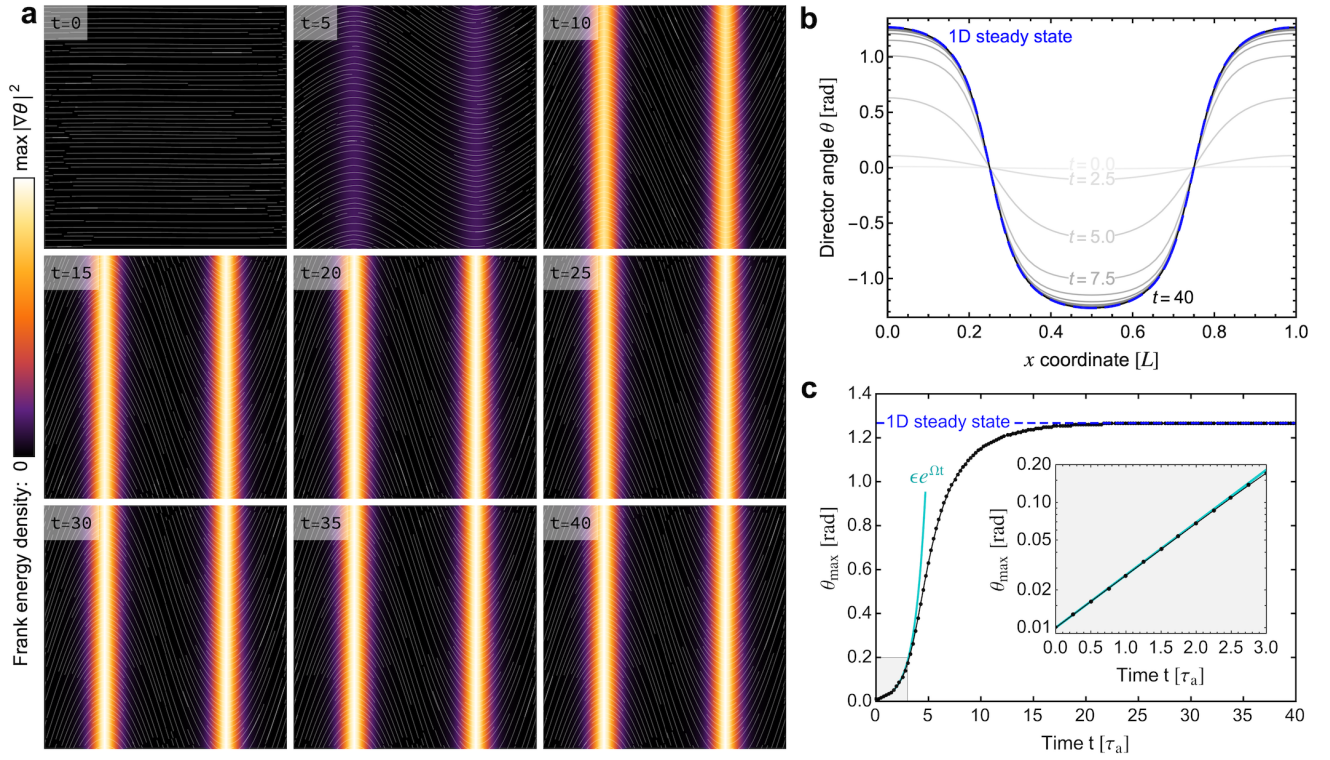
**Supplementary Figure 3 | Domain wall nodes in defect-free active nematics (expanded topology).** **a–c**, When walls are dominated by one type of distortion (either bend or splay), the possible nodes are startpoints (green, negative pseudo-defects), branchpoints (blue, negative pseudo-defects), and endpoints (red, positive pseudo-defects). **d**, Mergepoints (yellow, positive pseudo-defects) feature two incoming walls of the same type and one outgoing wall of the other type. While such combinations are topologically possible, they are not typically featured in our simulations.



**Supplementary Figure 4 | Skeleton detection and pseudo-defect classification.** **a**, Grayscale plot of the Frank free energy density, with black corresponding to  $|\nabla\theta|^2 = 0$  and white corresponding to  $|\nabla\theta|^2 \geq 0.5 \max |\nabla\theta|^2$  to facilitate binarization. **b**, Periodic expansion of (a) to avoid false detection of nodes along the original square boundaries (white outline). **c**, Local adaptive binarization of (b), followed by removal of small fragmented components not counted as walls. **d**, Recursive thinning of (c), then a step of dilation to fill up tiny gaps within some walls, an additional thinning step to recover the skeleton, and a pruning step to discard open branches shorter than a small threshold. **e**, Using the MorphologicalTransform tool we detect and highlight the skeleton nodes. **f**, We select only those nodes confined to the original periodic square. **g**, For the SkeletonEndPoints, we compute the vectors pointing outwards of their associated branch (black arrows) by finding the nearest neighbouring point on the wall skeleton. **h**, The wall polarity associated with each SkeletonEndPoint is shown in red (green) if its scalar product with (g) is positive (negative). **i**, Branchpoints (blue nodes), endpoints (red nodes) and startpoints (green nodes) are plotted with their orientation given by the local wall polarity.



**Supplementary Figure 5 | Labyrinths detection in arrested wall networks.** **a**, Grayscale plot of the Frank free energy density, with white corresponding to  $|\nabla\theta|^2 = 0$  and black corresponding to  $|\nabla\theta|^2 \geq 0.5 \max |\nabla\theta|^2$  to facilitate binarization. **b**, Periodic expansion of **(a)** to capture connected domains that meander through the periodic square boundaries. **c**, Local adaptive binarization of **(b)**, followed by a filling operator to discard isolated black fragments. **d**, Finding the connected morphological domains in **(c)**. **e**, Cropping out the periodic square domain from **(d)**. **f**, Applying our algorithm for relabeling domains that are connected through the left-right and top-bottom boundaries.



**Supplementary Figure 6 | Verification of the numerical scheme.** **a**, Consecutive snapshots from a simulation initiated with a small bending modulation about the uniformly aligned state:  $\theta(\mathbf{r}, t = 0) = \epsilon \cos(2\pi x)$ , with  $\epsilon = 0.01$ . Parameter values were set to  $R = 1$ ,  $\nu = -1.1$ ,  $A = 1000$ , and  $S = 1$  (extensile stress). Numerical parameters were set to  $N = 64$ ,  $dt = 0.01$ , and  $D = 0$  (zero noise). Color indicates the Frank energy,  $|\nabla\theta|^2$ , and white lines trace the director  $\mathbf{n}$ . **b**, We plot the numerical data corresponding to a horizontal slice,  $\theta(x, y = 0)$ , for increasing times, starting from  $t = 0$  (lightest gray) up to  $t = 40\tau_a$  (black) in intervals of  $2.5\tau_a$ . It is shown that the angle profile relaxes on the predicted 1D steady state (dashed blue), obtained for the same parameter values as explained in our recent work<sup>37</sup>. **c**, The maximum angle is plotted as function of time in our simulation (black). First, it is shown that the modulation grows exponentially in time with the growth rate  $\Omega$  matching the linear stability dispersion relation<sup>37</sup> (cyan). The gray inset is a log-scale plot comparing the simulation results with this explicit prediction for small perturbations. Additionally, it is demonstrated that the maximal angle in the simulation relaxes at long times to the value predicted by the 1D steady state<sup>37</sup> (dashed blue).

## SUPPLEMENTARY MOVIE CAPTIONS

**Supplementary Movie 1 | Strong large-scale turbulence in the contractile aligning regime.** The left panel shows the evolution of the flow field  $\mathbf{v}$ , with color indicating speed and black arrows representing streamlines. The right panel depicts the evolution of the Frank free energy density,  $|\nabla\theta|^2$ . The parameters are the same as in [Figs. 1a](#) and [1b](#), which are snapshots from the same simulation. The interval between movie frames is 500 computational time iterations, corresponding to a time interval of  $5\tau_a$ . The total duration of the Movie is  $2500\tau_a$ .

**Supplementary Movie 2 | Arrested turbulence in the extensile aligning regime.** The left panel shows the evolution of the flow field  $\mathbf{v}$ , with color indicating speed and black arrows representing streamlines. The right panel depicts the evolution of the Frank free energy density,  $|\nabla\theta|^2$ . The parameters are the same as in [Figs. 1d](#) and [1e](#), which are snapshots from the same simulation. The interval between movie frames is 500 computational time iterations, corresponding to a time interval of  $5\tau_a$ . The total duration of the Movie is  $2500\tau_a$ .

**Supplementary Movie 3 | Active turbulence in the absence of flow alignment (tumbling regime).** The left panel shows the evolution of the flow field  $\mathbf{v}$ , with color indicating speed and black arrows representing streamlines. The right panel depicts the evolution of the Frank free energy density,  $|\nabla\theta|^2$ . The parameters are the same as in [Extended Data Fig. 1a](#) and [1b](#), which are snapshots from the same simulation. The interval between movie frames is 500 computational time iterations, corresponding to a time interval of  $5\tau_a$ . The total duration of the Movie is  $2500\tau_a$ .

**Supplementary Movie 4 | Evolution from stripes to turbulence (contractile aligning vs extensile aligning).** The evolution of the Frank free energy density,  $|\nabla\theta|^2$ , in the contractile aligning case ( $S\nu = +1.1$ , left) and the extensile aligning case ( $S\nu = -1.1$ , right). The wavelength of the initial stripes—with splay walls on the left and bend walls on the right—was chosen to match the selected wavelength in the fully-developed turbulent state. In both cases, the stripes coarsen and then experience a ‘zigzag’ instability that folds the walls. In the contractile case (left), folded walls tend to dissolve and reappear perpetually. In the extensile case (right, [Fig. 2](#)), walls are more robust and tend to branch. As growing branches avoid other walls, the system reaches a grid-locked state that fluctuates only slightly. Parameters were set to  $R = 1$ ,  $\nu = -1.1$ , and  $A = 19692$  (chosen so that the system size roughly equals 6 times the selected wavelength). The interval between movie frames is 50 computational time iterations, corresponding to a time interval of  $1\tau_a$ . The total duration of the Movie is  $540\tau_a$ .

**Supplementary Movie 5 | Evolution of the wall-network skeleton and its nodes.** Skeleton of the domain walls (black) with startpoints, branchpoints and endpoints shown as green, blue and red triangular nodes, respectively (see [Fig. 3](#)). The detection of these structures is described in [Methods C](#) and [Extended Data Fig. 5](#). This movie demonstrates the pseudo-topological transitions mediating the ageing of an arrested wall network. Parameter values are as in [Fig. 5](#). The interval between movie frames is 500 computational time iterations, corresponding to a time interval of  $5\tau_a$ . The total duration of the Movie is  $1715\tau_a$ .

**SUPPLEMENTARY NOTE:  
TOPOLOGICAL PSEUDO-CHARGE OF DOMAIN WALL NODES**

In arrested and nearly arrested states, the domain walls are organized in a tree-like network. One can associate a planar, directed graph to this network, with three types of nodes: startpoints, endpoints, and branchpoints, as described in Figs. 3a to 3c. In the long-time asymptotics, the startpoints are only residual, and the ageing tree is mostly formed by endpoints and branchpoints (Fig. 5, Supplementary Movie 5). While these nodes are not topological defects of the nematic field, one can assign to them a pseudo-charge which is conserved and contains useful information of topological nature, as discussed in this section. We emphasize that this pseudo-topology is an effective emergent property of the dynamics, that holds only for the appropriate parameter regimes and time asymptotics. Therefore, pseudo-defects are dynamically stabilized but are not topologically stable in the sense that they can be removed by a continuous perturbation of the nematic field.

To define the topological pseudo-charge, we first consider the change of angle across a nematic wall. To this end, we look for steady-state solutions of the director field in 1D, that is, with translational invariance in the direction along the wall. In this case, the angle varies only along the transverse coordinate  $s$ . In the steady state, the director profile across the wall obeys the 1D stationary equation<sup>37</sup>

$$\ell_a^2 \partial_s^2 \theta = \frac{S(1 + \nu \cos 2\theta)(\sin 2\theta - \sin 2\bar{\theta})}{4 + R + R\nu^2 + 2R\nu \cos 2\theta}, \quad (\text{S1})$$

where  $\bar{\theta}$  is the orientation of the nematic director at the center of the domain wall. This equation supports sigmoidal angle profiles with an interface of thickness of the order of the active length  $\ell_a$  that continuously connects two plateaux of uniform angle. As the interfaces separate regions of uniform angle, they are referred to as domain walls, also called kinks and antikinks in other contexts.

For  $S\nu > -1$ , the two plateaux values of the nematic angle are  $\theta = \bar{\theta} \pm \frac{\pi}{2}$ , so the total rotation of the nematic across the wall is  $\Delta\theta = \pm\pi$ . For  $S\nu < -1$ , the plateaux angles correspond to the so-called Leslie angle defined by  $1 + \nu \cos 2\theta_L = 0$ , which amounts to an angle rotation of  $\Delta\theta = \pm(\pi - \arccos |\nu|^{-1})$  across the wall. We remark that the total angle variation across domain walls is independent of both the active length  $\ell_a$  and the viscosity ratio  $R$ . For a domain wall centered at  $s = s_i$ , we define the smooth step functions  $\Theta^\pm(s - s_i)$  that connect the plateaux values via a total angle increment  $\Delta\theta$ , which is positive for  $\Theta^+$  and negative for  $\Theta^-$ . The angle varies at a scale  $\sim \ell_a$  about  $s_i$ . Similarly, the derivative with respect to the spatial coordinate  $s$  defines two peaked functions  $\dot{\Theta}^\pm(s - s_i)$  such that, in the sharp-wall limit,

$$\lim_{\ell_a \rightarrow 0} \dot{\Theta}^\pm(s - s_i) = \Delta\theta \delta(s - s_i) \equiv \pm \frac{Q(\nu)}{2\pi} \delta(s - s_i). \quad (\text{S2})$$

Here,  $Q(\nu)$  is the elementary pseudo-charge function, defined

as

$$Q(\nu) \equiv \frac{1}{2\pi} \int_{-\infty}^{+\infty} \dot{\Theta}_0^+ ds > 0, \quad (\text{S3})$$

which gives, for  $S\nu < 0$ ,

$$Q(\nu) = \frac{1}{2} \left( 1 - \frac{1}{\pi} \mathcal{H}(|\nu| - 1) \arccos |\nu|^{-1} \right) > 0, \quad (\text{S4})$$

where  $\mathcal{H}$  is the Heaviside step function. The elementary pseudo-charge function  $Q(\nu)$  takes the value 1/2 in the tumbling regime, and it spans the interval from 1/2 to 1/4 as  $|\nu|$  is increased beyond 1. The functional form of  $Q(\nu)$  is plotted in Fig. S1.

To define a topological pseudo-charge of the pseudo-defects, and of any closed domain in general, we recall that the total angle variation along a closed loop must be

$$\oint d\theta = \oint \dot{\theta} ds = 0, \quad (\text{S5})$$

with  $\dot{\theta} ds = \vec{\nabla} \theta \cdot d\vec{s}$  where  $d\vec{s}$  describes the contour, with  $s$  the arclength coordinate. We are interested in the limit of small  $\ell_a$ , or equivalently, to situations where the separation between consecutive walls is much larger than the wall thickness, so that there is no significant overlap between  $\dot{\Theta}^\pm(s - s_i)$  and  $\dot{\Theta}^\pm(s - s_j)$ , i.e.  $|s_i - s_j| \gg \ell_a$ . Then, we can distinguish two scales of variation of the nematic orientation: the inner region of the domain wall where the nematic variation is fast ( $\dot{\theta} \sim \ell_a^{-1}$ ), and the outer regions where it is slow ( $\dot{\theta} \sim \ell_a^0$ ). Under these circumstances, we may define the pseudo-charge as the part of the director rotation along a closed loop that takes place at the slow-variation (outer regions of the domain walls). In other words, we consider the total director rotation excluding the fast variation across the walls that are intersected by the loop.

Consider, for instance, an isolated endpoint pseudo-defect (Fig. 3c), formed by a wall that points towards it, and consider a counterclockwise closed path  $\Gamma$  that contains it and intersects the center of the wall at  $s = s_0$ . We define the pseudo-charge of this pseudo-defect as

$$Q_\Gamma = \frac{1}{2\pi} \oint_\Gamma \left( \dot{\theta}(s) - \dot{\Theta}^-(s - s_0) \right) ds \quad (\text{S6})$$

$$= \frac{1}{2\pi} \oint_\Gamma \dot{\Theta}^+(s - s_0) ds > 0, \quad (\text{S7})$$

which coincides strictly with  $Q(\nu)$  in the sharp-wall limit. To subtract the localized fast variation of  $\theta$  across the wall we need to write  $\dot{\Theta}^-(s - s_0)$  because the nematic is rotating clockwise across the wall (decreasing angle), if the wall is oriented towards the interior of the path that encloses the endpoint. In general, the sense of rotation of the nematic across a wall is opposite (equal) to the sense of rotation of the closed

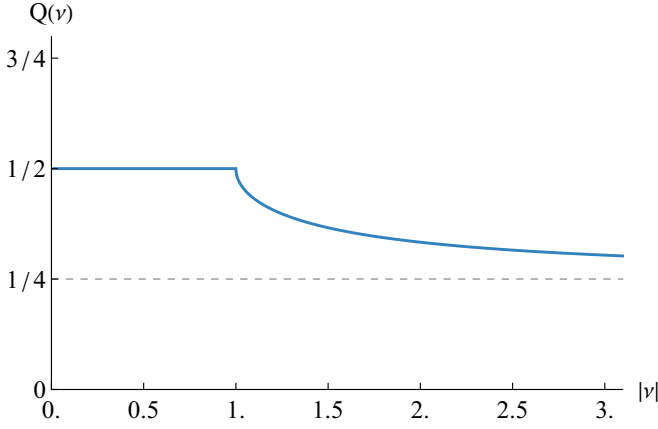


**Figure S1** |  $Q$  as a function of  $|\nu|$ . Functional form of the elementary charge  $Q(\nu)$ . Positive pseudo-defects have charge  $+Q$ , and negative ones  $-Q$ . For the tumbling regime  $Q = 1/2$  and for the aligning regime  $Q$  decreases monotonically from  $1/2$  to  $1/4$ .

loop when the wall points towards the interior (exterior) of the loop.

Similarly, for an isolated branchpoint we define the pseudo-charge as the rotation of the director in regions excluding the walls along a closed loop enclosing the branchpoint (Fig. 3b). In this case, we must subtract the fast variation across the three walls intersected by the integration path. Since there is always one wall pointing towards the interior and two pointing towards the exterior, the pseudo-charge for a branchpoint, in the sharp-wall limit, will be  $-Q(\nu)$ .

For a general configuration with an arbitrary number of pseudo-defects and associated walls, the total pseudo-charge in the interior of a closed loop will given by the sum of the pseudo-charge of all the pseudo-defects in it. We remark that it is not necessary to know the detailed structure of the nematic field in the interior, but only in the contour, as in the definition of the actual topological charge. In fact, the total pseudo-charge in the interior of an arbitrary closed loop  $\Gamma$  is

also given by

$$Q_{\Gamma} = (m_{\text{in}} - m_{\text{out}})Q(\nu), \quad (\text{S8})$$

where  $m_{\text{in}}$  and  $m_{\text{out}}$  are the number of inward and outward domain walls crossed by the contour line, respectively.

In the case of domain walls with a small but finite thickness compared to typical wall separation, the elementary pseudo-charge will slightly differ from the limiting value defined in Eq. (S3). In that case, consecutive walls partially overlap so that the angle profile does not reach the asymptotic value of the plateau, and the magnitude of the angle variation across the walls,  $\Delta\theta$ , is slightly smaller. This is the case in the wall patterns studied in this work, so in the main manuscript we refer to the values taken by the pseudo-topological charge only as  $\simeq Q(\nu)$ . We remark, however, that the precise value of the elementary charge  $Q(\nu)$  is not really informative of the relevant topological structure, that is, how walls are connected, but accounts for the detailed structure of the walls themselves. This may be important to determine their dynamical properties, such as their interactions or their rigidity to deformation. However, it is only the integer counts of positive and negative pseudo-defects (or the counts of inward and outward wall intersections), i.e., the multiples of the elementary charge, that are informative of the overall qualitative structure inside a given domain.

In the sharp-wall limit  $\ell_a \rightarrow 0$ , the idea of a pseudo-defect is reminiscent of Dirac's construction of magnetic monopoles, based on attaching to them the so-called Dirac string, which carries a quantized magnetic flux<sup>48</sup>. In that way, the magnetic monopole can be made consistent with Maxwell's equations. For instance, the total magnetic flux across a closed surface enclosing the magnetic monopole would be zero, as required by Gauss' theorem for the absence of net magnetic charge, because the flux generated by the monopole is canceled by that carried out by the string, which also crosses the surface. Similarly, in our problem, the wall attached to the pseudo-defect provides a localized (fast) rotation of the director that cancels the (slow) rotation outside the wall to ensure the lack of true topological charge. In this way, the problem satisfies the local constraint of zero topological charge while mimicking with pseudo-defects the director field around actual topological defects in a large region of space around them.